



High-performance organic pseudocapacitors via molecular contortion

Jake C. Russell¹, Victoria A. Posey¹, Jesse Gray¹, Richard May², Douglas A. Reed¹, Hao Zhang³, Lauren E. Marbella², Michael L. Steigerwald¹, Yuan Yang⁴, Xavier Roy¹, Colin Nuckolls¹ and Samuel R. Peurifoy¹

Pseudocapacitors harness unique charge-storage mechanisms to enable high-capacity, rapidly cycling devices. Here we describe an organic system composed of perylene diimide and hexaazatrinaphthylene exhibiting a specific capacitance of 689 F g⁻¹ at a rate of 0.5 A g⁻¹, stability over 50,000 cycles, and unprecedented performance at rates as high as 75 A g⁻¹. We incorporate the material into two-electrode devices for a practical demonstration of its potential in next-generation energy-storage systems. We identify the source of this exceptionally high rate charge storage as surface-mediated pseudocapacitance, through a combination of spectroscopic, computational and electrochemical measurements. By underscoring the importance of molecular contortion and complementary electronic attributes in the selection of molecular components, these results provide a general strategy for the creation of organic high-performance energy-storage materials.

The development of energy-storage materials has traditionally focused on costly metal-containing solids¹. Recent successes in fully organic energy-storage materials² have galvanized interest in lightweight, affordable and high-performance solutions for meeting globally increasing energy demands³. Pseudocapacitors bridge the gap between secondary batteries and supercapacitors, leveraging a combination of electrical double-layer capacitance and surface-level Faradaic redox processes to store and release charge at rapid rates⁴. As a result, pseudocapacitors can provide higher power than batteries and higher energy density than supercapacitors. However, most high-performance pseudocapacitors are fabricated from metal oxides, often requiring transition metals that are not Earth-abundant⁴. Fully organic pseudocapacitors are an inexpensive and green alternative, but until now, they have underperformed compared with their inorganic counterparts⁵. These limitations are especially salient for electron-accepting materials used in negative electrodes, which are required for pairing with electron-donating materials in positive electrodes to achieve maximum performance in asymmetric cells^{6,7}.

Here we report an extraordinarily high pseudocapacitive performance from PHATN (perylene diimide–hexaazatrinaphthylene), an organic network fabricated from perylene diimide (PDI) and hexaazatrinaphthylene (HATN), whose synthesis and characterization are demonstrated in this work. These complementary molecular units were selected for their unique structures and robust electrochemical properties. PDIs are common and inexpensive industrial pigments⁸. Their use in electrochemical systems has been investigated extensively due to their notable stability, ease of derivatization and ability to reversibly accept electrons⁹. HATN is a planar aromatic molecule exhibiting a high density of electroactive moieties¹⁰ and synthetic flexibility¹¹. In the design of PHATN, we demonstrate two major principles that may be generalized to other organic materials: (1) the selection of complementary electroactive

components, in which each expands the voltage range and thus the charge-storage capacity of the system, and (2) the contortion of the aromatic surface participating in the pseudocapacitive behaviour, which opens space for electrolyte and ion movement, leading to enhanced rate capability.

Figure 1a summarizes the material synthesis (see Methods for details). The polymerization of PDI and HATN building blocks into the scaffold PHATN utilizes a facile two-step strategy (Fig. 1a,b) based on Suzuki cross-coupling (Fig. 1c) followed by visible-light flow photocyclization (Fig. 1d)¹². The PDI building block is initially decorated with alkyl chains (R) to facilitate solution processing. Once formed into the polymeric framework, these chains are removed via vacuum thermolysis, as shown by thermogravimetric analysis and gas chromatography-mass spectrometry of the condensate (Supplementary Figs. 5 and 6, respectively). Both ¹³C solid-state NMR (ssNMR) and infrared spectroscopy confirm near-quantitative removal of the alkyl chains (Extended Data Fig. 1a and Supplementary Fig. 7a) and retention of the imide moiety (Supplementary Fig. 7b). The resulting material (Fig. 1e) achieves best-in-class capacitance values of 689 F g⁻¹ at a current density of 0.5 A g⁻¹ and performs well even at extremely high current densities (75 A g⁻¹), yielding capacitance values of over 430 F g⁻¹. These values are the highest of any reported negative-electrode (that is, electron-accepting) organic pseudocapacitor material and outperform even well-established positive organic pseudocapacitor architectures (Fig. 1f). To demonstrate a practical implementation of this material, we fabricated two-electrode hybrid energy-storage cells from PHATN using activated carbon (AC) as the cathode; these cells display impressive specific energy and power. Overall, we find that the mechanistic origin of PHATN's performance is the prevalence of surface-level redox events that are directly attributable to the molecular design principles outlined above.

¹Department of Chemistry, Columbia University, New York, NY, USA. ²Department of Chemical Engineering, Columbia University, New York, NY, USA.

³Department of Chemistry, Beijing Key Laboratory of Advanced Chemical Energy Storage Technologies and Materials, Beijing, China. ⁴Department of Applied Physics and Applied Mathematics, Columbia University, New York, NY, USA. ✉e-mail: xr2114@columbia.edu; cn37@columbia.edu; s.peurifoy@columbia.edu

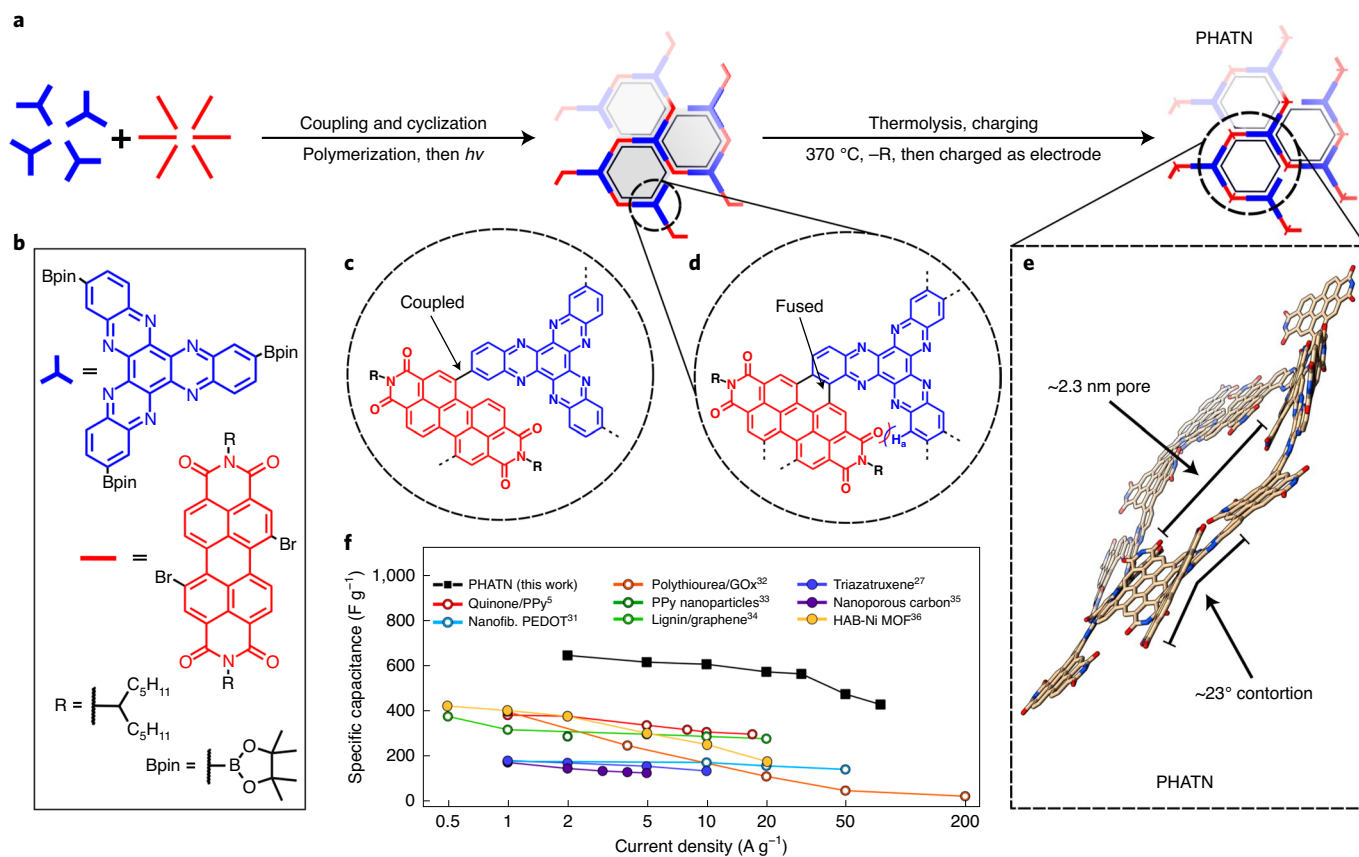


Fig. 1 | Synthesis, structure and performance of the electroactive polymer PHATN. **a**, Design employed in the fabrication of PHATN. Opacity offset indicates the three-dimensional nature of the helical network. **b**, Key for building blocks. **c**, PDI (red) is coupled to a three-pronged HATN scaffold (blue). **d**, The network is cyclized using a visible-light flow photocyclization reaction. The resulting material is thermolysed to free the electroactive polymer from the insulating alkyl chains. **e**, Density functional theory representation of an idealized pore of PHATN, with an approximate idealized pore diameter of 2.3 nm. The calculated angle of contortion for this structure is $\sim 23^\circ$. The material exhibits a contorted conformation due to steric hindrance from the imide position (see hydrogen labelled H_a in **d**). **f**, Specific capacitance (C_s) versus current density for PHATN (black) and other recently reported organic pseudocapacitor materials. Filled symbols represent negative-electrode materials, and open symbols represent positive-electrode materials. See refs. ^{5,16,31–36} for the compared systems and Extended Data Fig. 3 for a more comprehensive chart that includes a wider range of inorganic and hybrid materials. PPy, polypyrrole; nanofib., nanofibrillar; PEDOT, poly(3,4-ethylenedioxythiophene); GOx, graphene oxide; HAB, hexaaminobenzene; MOF, metal-organic framework.

The key structural feature underpinning the performance of PHATN is the contortion of the aromatic system, which simultaneously improves its ion mobility, exposed surface for ion association and processability. These features are in sharp contrast with traditional planar systems in which strong π -stacking disrupts solubility and hinders ion mobility. The concept of molecular contortion is well-established within the field of organic electronics^{13,14}. These established principles¹⁵ are used to support our conclusions of contortion within PHATN and explain the resulting emergent properties. The contortion of the aromatic system was spectroscopically and theoretically studied using a soluble model compound composed of one HATN unit and three PDI units (PHATN monomer, structure shown in Supplementary Scheme 4), as well as with an uncontorted control material, as discussed later in the manuscript. NMR spectroscopy of the PHATN monomer (Supplementary Figs. 3 and 4) confirms the position of the cyclization, and density functional theory (DFT) calculations reveal the contorted helical character of the structure (Extended Data Fig. 2 and Supplementary Figs. 29 and 30). Although PHATN is composed of two planar aromatic systems, steric interaction at the imide position and a proximal hydrogen on the HATN linker (labelled H_a in Fig. 1d) force the aromatic network out of planarity.

To evaluate the electrochemical behaviour of this new material, we fabricated working electrodes by drop casting onto carbon

paper a slurry of PHATN, carbon black (as conductive agent) and polytetrafluoroethylene (PTFE; as binder) in a mass ratio of 8:1:1 suspended in *N*-methyl-2-pyrrolidone. We utilized a three-electrode setup comprising the PHATN working electrode, a graphite counter electrode and a Hg/HgO reference electrode, all suspended in 6 M KOH aqueous electrolyte. The PHATN electrode was presoaked in electrolyte under vacuum to ensure full infiltration of the pores. During this process, the imide carbonyl groups associate with the K^+ ions in solution, as indicated by a shift of the carbonyl ^{13}C ssNMR resonance to higher frequency upon soaking (Extended Data Fig. 1b). Note that the ^{13}C ssNMR chemical shift upon K^+ -ion association is remarkably large, a consequence of the molecular contortion^{16,17}. In addition, the contortion of PHATN produces an easily accessible internal surface area, as demonstrated by the large Brunauer–Emmett–Teller surface area of $131 \text{ m}^2 \text{ g}^{-1}$ calculated from the gas adsorption isotherms collected using CO_2 (Extended Data Fig. 4). Together, the ^{13}C ssNMR and gas adsorption isotherm measurements support the contortion model and resulting pore-infiltration hypothesis.

Cyclic voltammetry (CV) of the PHATN electrode reveals broad and overlapping reduction peaks at -0.7 and -1.0 V versus Hg/HgO (Fig. 2a,b). These fully reversible peaks originate from the sequential reductions of the PDI and HATN units. To confirm this assignment,

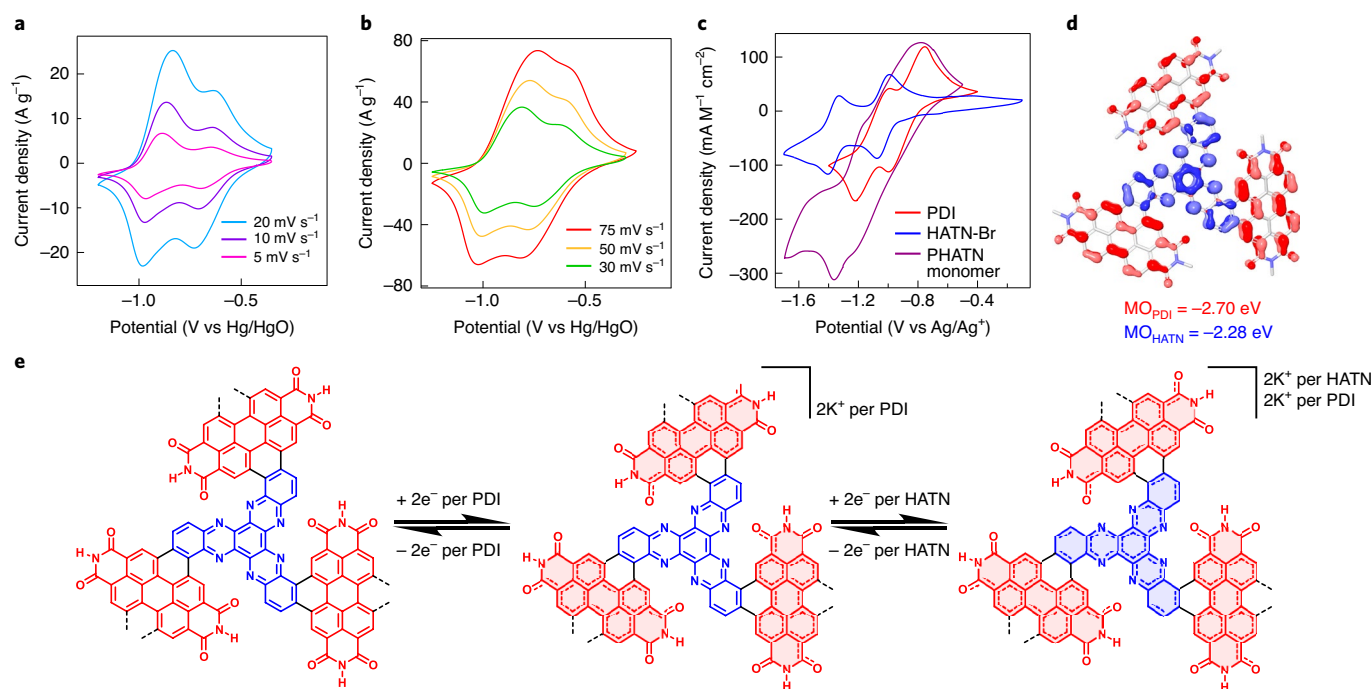


Fig. 2 | Three-electrode CV and charging mechanism of PHATN. **a, b** Three-electrode CV of PHATN showing broad and reversible reduction peaks at low (**a**) and high (**b**) rates. The electrolyte is a 6 M KOH aqueous solution. **c**, Solution-phase cyclic voltammograms of individual PHATN building blocks show two distinct reductions each, overlapping with the PHATN monomer. The current densities of HATN-Br and the PHATN monomer are scaled to match the concentration of PDI (0.01 M). The electrolyte is 0.1 M TBA-PF₆ in DCM. TBA-PF₆, tetrabutylammonium hexafluorophosphate; DCM, dichloromethane. **d**, Unoccupied molecular orbital (MO) levels of the building blocks. Three degenerate MOs comprise the total PDI visualization and a single MO comprises the HATN visualization. The PDI moieties are reduced before the HATN moieties. Lighter MOs indicate opposing phases. **e**, Proposed mechanism for charge storage within the extended PHATN system. Reversible reduction events store two electrons per PDI (red) followed by two electrons per HATN (blue) moiety.

we investigated the individual redox processes by performing CV experiments on PDI, HATN-Br and the PHATN monomer in solution (Fig. 2c). Both PDI and HATN-Br display two clear reduction peaks, with the pair for HATN-Br at a slightly more negative potential^{11,18}. The cyclic voltammogram of the PHATN monomer can be understood as a convolution of these two behaviours. These observations are supported by DFT of the PHATN monomer: the levels associated with the PDI moieties are more energetically accessible than those associated with the HATN moieties (Fig. 2d). Figure 2e illustrates the charge-storage mechanism of PHATN: the PDI moiety first accepts two electrons¹⁹, then the HATN moiety accepts two more^{11,20}. The charges are delocalized across their respective π -systems, giving rise to the observed broad and overlapping peaks. This mechanism leads to a calculated theoretical specific capacitance of 996 F g⁻¹ for PHATN.

To understand the remarkable charge-storage kinetics of PHATN and demonstrate its capacitive behaviour, we performed CV at different sweep rates (1–300 mV s⁻¹). The reduction peaks display a slight anodic shift with respect to the oxidation peaks. When intercalation kinetics are at play in battery materials, this shift is often greater than 0.1 V, even at rates as low as 0.1 mV s⁻¹, and increases dramatically at higher rates²¹, leading to reduced energy efficiency. By contrast, pseudocapacitors are kinetically limited at low rates only by the speed of the surface-level Faradaic (that is surface-controlled) reactions, and at higher rates by electrolyte diffusion. Figure 3a shows the peak separation of the first redox event in PHATN as a function of the sweep rate. At low rates, the peaks are nearly coincident (separation < 0.05 V) and the separation increases slowly with sweep rate, indicating surface-limited redox behaviour^{21,22}. Above a critical rate of ~50 mV s⁻¹, the peak shift increases more dramatically as the system reaches diffusion-limited behaviour.

Figure 3b displays a log–log plot of the sweep rate (ν) versus the peak current (i). These parameters obey the power law given in equation (1):

$$i \propto \nu^b \quad (1)$$

where the slope of the linear fit of the log–log plot is b . From the lowest rate up to 50 mV s⁻¹, the slope b of the linear fit is 0.98. A value near unity indicates purely surface-controlled behaviour, while $b=0.5$ implies diffusion-controlled Randles–Ševčík behaviour²³. Above 50 mV s⁻¹, the slope decreases to 0.72, suggesting a rate limitation that arises from diffusion constraints. That the surface-controlled regime extends to such high rates supports the pseudocapacitive behaviour and explains the exceptionally good performance of PHATN at fast charging speeds.

The relationship between the capacity (Q) and sweep rate provides further evidence for surface-mediated charge storage in PHATN. Figure 3c displays a plot of Q versus $\nu^{-1/2}$. Sweep rates below 50 mV s⁻¹ have purely surface-controlled kinetics, whereas higher sweep rates are limited by diffusion. By taking a linear extrapolation of this surface-controlled region to $\nu = \infty$, the infinite sweep rate capacity can be estimated, which corresponds to the ‘outer’ charge of the material, that is easily accessible by the electrolyte^{24–26}. Similarly, a plot of $1/Q$ versus $\nu^{1/2}$ (Fig. 3d) can be extrapolated to $\nu=0$ to estimate the ‘total’ charge, which includes areas shielded from the electrolyte. Here, the outer charge is estimated at 105 mAh g⁻¹, representing 60% of the total charge, which is 174 mAh g⁻¹. This ratio indicates that a majority of the charge capacity of the material is found in electrolyte-accessible regions and is due to surface processes. Together, these results support rapid surface-level redox activity as the source of the material’s high rate

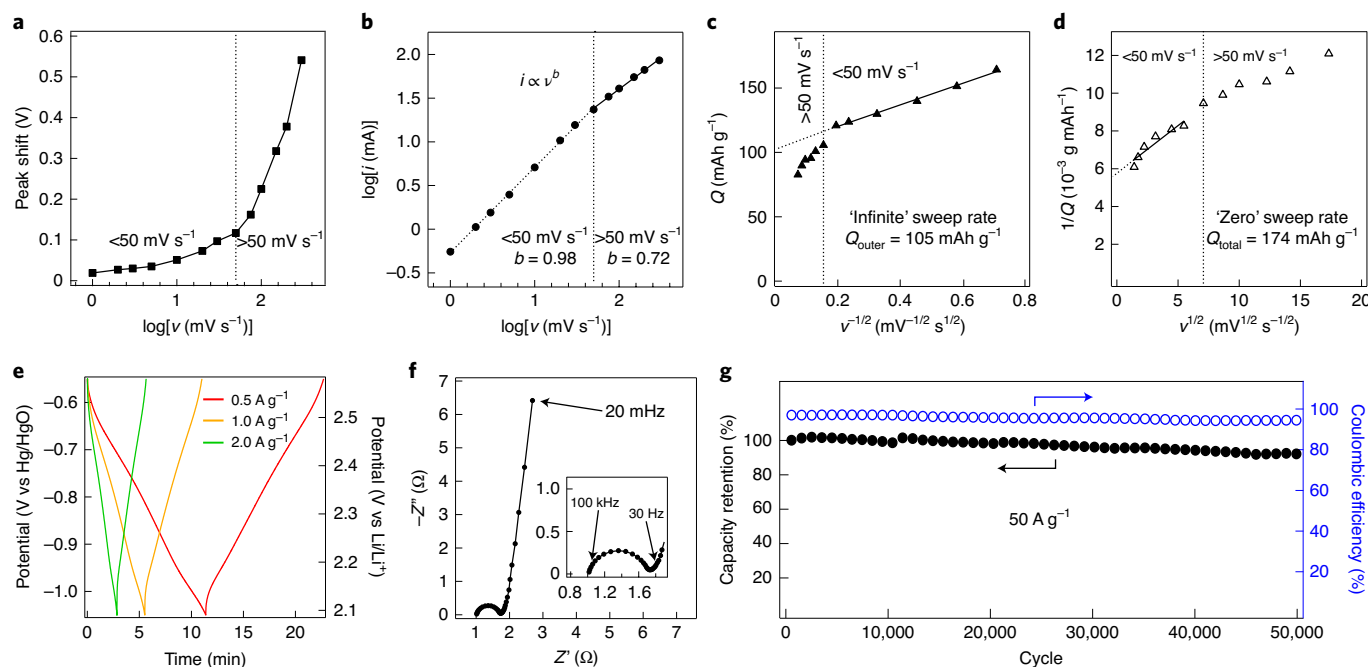


Fig. 3 | Three-electrode electrochemical characterization of pseudocapacitive behaviour and kinetics of PHATN. a, Anodic peak shift of the first redox couple at different sweep rates, showing small shifts at rates below 50 mV s^{-1} . **b**, log-log plot of peak current versus sweep rate, showing a slope near unity below 50 mV s^{-1} . **c**, Q versus $v^{-1/2}$, with extrapolation to $v = \infty$ to estimate the outer charge storage. **d**, $1/Q$ versus $v^{1/2}$, with extrapolation to $v = 0$ to estimate the total charge storage. **e**, Three-electrode GCD cycling of PHATN at different current densities exhibiting the triangular shape characteristic of pseudocapacitors. **f**, Nyquist plot from 100 kHz to 20 mHz shows a small semicircle at high frequency and a steep Warburg slope at low frequency. **g**, Cycling stability over $50,000$ cycles at a current density of 50 A g^{-1} . The left axis (black, filled circles) displays capacity retention, and the right axis (blue, open circles) displays coulombic efficiency. Measurements in **a–g** were performed in 6 M KOH aqueous electrolyte.

capability. As discussed below, this high rate capability is enabled by molecular contortion, which permits both long-range conjugation and highly accessible areas for redox activity.

Figure 3e shows galvanostatic charge–discharge (GCD)²⁷ curves of the material in a three-electrode setup, at current densities ranging from 0.5 to 2 A g^{-1} . The triangular shape characteristic of capacitor-like materials is obvious. We note that at lower currents, the electrolysis of water begins to dominate the reduction cycle, lowering the coulombic efficiency. From the GCD data, we calculate specific capacitance using equation (2):

$$C_s = \frac{I \times t}{\Delta E} \quad (2)$$

where I is current density, t is cycle time and ΔE is the potential difference between the top and bottom of the cycle. At 0.5 A g^{-1} , we measure an extremely high capacitance of 689 F g^{-1} , far surpassing comparable organic pseudocapacitor materials, both negative and positive electrodes alike (Fig. 1f and Extended Data Fig. 3). This value is 69% of the theoretical capacitance (996 F g^{-1}), in agreement with the Q – v analysis, and suggests that an even better performance could be achieved with further device optimization and nanostructuring²⁸. The capacitance decreases at higher cycling rates, as expected from the kinetic limitations detailed above, but even at the highest measured current density of 75 A g^{-1} , PHATN retains a performance of 432 F g^{-1} (Supplementary Table 3).

We measured the impedance of the system at different frequency (f) values using electrochemical impedance spectroscopy (EIS). Figure 3f displays the Nyquist plot of PHATN collected at -0.7 V versus Hg/HgO . The high-frequency region, from 100 kHz to 30 Hz , shows a semicircular shape with a diameter of $\sim 0.8 \Omega$, indicating very low interfacial charge-transfer resistance (R_{ct})²⁹.

The high-frequency x -intercept of the curve represents the equivalent series resistance (ESR, R_s) of the entire system, $\sim 1 \Omega$. Finally, the low-frequency region corresponds to the Warburg impedance (Z_w), with the near-vertical slope indicating fast diffusion of ions towards the electrode surface. The specific capacitance as a function of frequency can also be calculated from EIS data using equation (3):

$$C(f) = -\frac{1}{2\pi \times m \times Z'' \times f} \quad (3)$$

where m is the mass of the active material on the electrode and Z'' is the imaginary component of the resistance.

A value of around 800 F g^{-1} is achieved at the lowest frequencies, while capacitance values of 400 and 200 F g^{-1} are retained even at 1 and 10 Hz , respectively (Extended Data Fig. 5c). We also tested the cycling stability of PHATN at a high current density of 50 A g^{-1} (Fig. 3g and Supplementary Fig. 10c) and observed an 8% decrease in capacitance and no decrease in coulombic efficiency over $50,000$ cycles. Another device was cycled $10,000$ times at 20 A g^{-1} , with a 3% decrease in capacitance (Supplementary Fig. 10b). Self-discharge measurements show a behaviour comparable to other organic supercapacitor materials, retaining 84% capacity after 3 h (Extended Data Fig. 6). The retained capacity increases to 99% after 3 h when the electrode is held at -1.0 V for 10 min before the self-discharge test.

To conclusively demonstrate the efficacy of the contortion design, we synthesized a planar analogue of PHATN composed of alternating phenazine and PDI units (PA-PDI). Phenazine emulates the structure and electrochemical properties of HATN, but, as opposed to the tritopic contorted HATN, it cyclizes with PDI to form a planar linear structure (Supplementary Scheme 6). The cyclic voltammogram of PA-PDI resembles that of PHATN

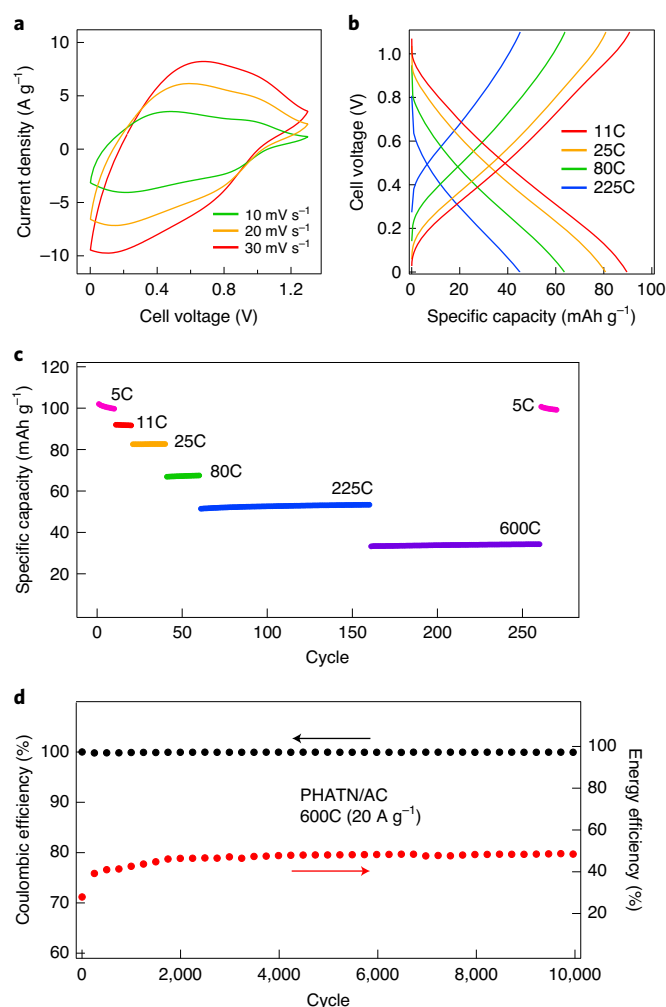


Fig. 4 | Characterization of two-electrode button cells assembled from PHATN(–) and AC(+) electrodes. **a**, CV of the device, showing overall rectangular shape and a suggestion of the two redox peaks characteristic of PHATN. **b**, Charge–discharge curves of the PHATN/AC cell showing substantial capacity, even at extremely high C-rates. **c**, Capacity retention of the PHATN/AC cell at sequentially higher C-rates. After GCD cycling up to an extremely high rate of 600C, the rate can be lowered back to 5C while maintaining the original capacity. **d**, Coulombic efficiency and energy efficiency of the PHATN/AC device over 10,000 cycles at a rate of 600C (20 A g^{–1}). Energy efficiency is low due to the relatively low voltage of the PHATN/AC cell. Measurements in **a–d** were performed using 6 M KOH aqueous electrolyte with a PHATN electrode mass loading of 6.4 mg cm^{–2}.

(Extended Data Figs. 7a and 8a) but its capacitance is notably lower (for example, 100 F g^{–1} at 10 A g^{–1}; Extended Data Fig. 9a) and the shallower Warburg slope from EIS indicates a less capacitive behaviour (Extended Data Fig. 8c). The cycling performances of PA-PDI and PHATN are comparable, underlining the general and outstanding stability of the structures produced by coupling PDI and annulated pyrazines (for example PA and HATN; Extended Data Fig. 9b). The key difference is that the diffusion coefficient of ions in PHATN is almost one order of magnitude larger than in PA-PDI, as measured by the galvanostatic intermittent titration technique (GITT; Extended Data Fig. 10). Consistent with this result, gas adsorption isotherms in PA-PDI reveal a much smaller surface area (12 m² g^{–1}) than in the contorted PHATN (Extended Data Fig. 4). Overall, we attribute these differences to the contortion of PHATN. Namely, (1) contortion improves the accessible surface area³⁰ to facilitate

ion diffusion, (2) contortion improves solubility by preventing π – π stacking during synthesis¹⁴, which may in turn lead to larger molecular weight polymers, and (3) contortion enables cavity-like and bowl-like shape-matching for potential guest ions to easily bind in a stable and reversible fashion¹⁵.

Taken together, the results presented here indicate that PHATN holds potential as a practical electrode material, leading us to further investigate its use in a realistic device architecture. Using PHATN, we constructed and tested two-electrode capacitor devices. We assembled several different architectures of two-electrode cells, using PHATN and AC as the negative and positive electrodes, respectively (full results are in Supplementary Figs. 12–22 and Supplementary Tables 5–7). To highlight the versatility of PHATN as a negative electrode, we also fabricated two-electrode ‘hybrid’ devices using Ni(OH)₂ as the positive electrode, which shows a similar performance to AC (discussed in Supplementary Figs. 23–27). CV of the AC-based two-electrode cell produces a similar shape to that seen in the three-electrode measurements, with multiple broad overlapping peaks (Fig. 4a). While the contribution of the AC electrode causes some expected asymmetry between the cathodic and anodic peaks, the accessible voltage window is extended to 1.3 V, much higher than for the individual PHATN electrode.

Charge–discharge measurements (Fig. 4b) confirm that the high rate capability of PHATN is maintained in the two-electrode devices. At the lowest rate of 5C (0.5 A g^{–1}), we measure a capacity of 103 mAh g^{–1}, slightly less than that found in the single electrode. Even at the extraordinarily high rate of 600C (20 A g^{–1}), the cell still displays a capacity of over 30 mAh g^{–1} and is able to return to lower rates without a loss of performance (Fig. 4c). Furthermore, the cell has good cycling stability at high rates, cycling 10,000 times at 600C with near 100% coulombic efficiency (Fig. 4d) and no loss in capacity (Supplementary Fig. 15).

In summary, we have demonstrated a robust organic material composed of PDI and HATN exhibiting best-in-class energy-storage properties among organic pseudocapacitor materials. Displaying single-electrode capacitance of nearly 700 F g^{–1} in aqueous electrolyte and high performance at current densities of up to 75 A g^{–1} over tens of thousands of cycles, this system pushes the boundaries of organic energy-storage materials. These properties are a direct consequence of our design principles: (1) the combination of complementary organic components, which increase the total available energy and potential window, and (2) molecular contortion to permit both facile diffusion and long-range charge delocalization. Such characteristics combine synergistically to promote rapid charging, high capacitance and long-term stability. Future designs could explore the use of larger polycyclic aromatic hydrocarbon fragments, such as coronene, decorated with electronically tunable edge groups and cyclized onto a three-pronged scaffold such as triptycene or hexaazatrinaphthylene. Taken together, these results advance our fundamental understanding of the design characteristics necessary to achieve high-performance pseudocapacitors, and underpin promising developments in the search for affordable, organic, high-power energy-storage solutions.

Online content

Any methods, additional references, Nature Research reporting summaries, source data, extended data, supplementary information, acknowledgements, peer review information; details of author contributions and competing interests; and statements of data and code availability are available at <https://doi.org/10.1038/s41563-021-00954-z>.

Received: 10 March 2020; Accepted: 9 February 2021;
Published online: 01 April 2021

References

- Schmidt, O., Hawkes, A., Gambhir, A. & Staffell, I. The future cost of electrical energy storage based on experience rates. *Nat. Energy* **2**, 17110 (2017).
- Lu, Y. & Chen, J. Prospects of organic electrode materials for practical lithium batteries. *Nat. Rev. Chem.* **4**, 127–142 (2020).
- Pomerantseva, E., Bonaccorso, F., Feng, X., Cui, Y. & Gogotsi, Y. Energy storage: the future enabled by nanomaterials. *Science* **366**, eaan8285 (2019).
- Choi, C. et al. Achieving high energy density and high power density with pseudocapacitive materials. *Nat. Rev. Mater.* **5**, 5–19 (2019).
- Kim, S. K., Cho, J., Moore, J. S., Park, H. S. & Braun, P. V. High-performance mesostructured organic hybrid pseudocapacitor electrodes. *Adv. Funct. Mater.* **26**, 903–910 (2016).
- Boota, M. & Gogotsi, Y. MXene—conducting polymer asymmetric pseudocapacitors. *Adv. Energy Mater.* **9**, 1802917 (2019).
- Bryan, A. M., Santino, L. M., Lu, Y., Acharya, S. & D'Arcy, J. M. Conducting polymers for pseudocapacitive energy storage. *Chem. Mater.* **28**, 5989–5998 (2016).
- Faulkner, E. B. & Schwartz, R. J. *High Performance Pigments* 2nd edn (Wiley, 2009).
- Lee, S. K. et al. Electrochemistry, spectroscopy and electrogenerated chemiluminescence of perylene, terylene, and quaterylene diimides in aprotic solution. *J. Am. Chem. Soc.* **121**, 3513–3520 (1999).
- Geng, J., Renault, S., Poizot, P. & Dolhem, F. Search for greener Li-ion batteries: an alternative offered by organic electroactive materials. in *Energy Harvesting and Storage: Materials, Devices, and Applications II* (eds Dhar, N. K. et al.) 803504 (SPIE, 2011).
- Peng, C. et al. Reversible multi-electron redox chemistry of π -conjugated N-containing heteroaromatic molecule-based organic cathodes. *Nat. Energy* **2**, 17074 (2017).
- Peurifoy, S. R. et al. Three-dimensional graphene nanostructures. *J. Am. Chem. Soc.* **140**, 9341–9345 (2018).
- Schuster, N. J. et al. Electron delocalization in perylene diimide helicenes. *Angew. Chem. Int. Ed.* **128**, 13717–13721 (2016).
- Zhong, Y. et al. Helical ribbons for molecular electronics. *J. Am. Chem. Soc.* **136**, 8122–8130 (2014).
- Peurifoy, S. R. et al. Dimensional control in contorted aromatic materials. *Chem. Rec.* **19**, 1050–1061 (2019).
- Forse, A. C., Griffin, J. M., Presser, V., Gogotsi, Y. & Grey, C. P. Ring current effects: factors affecting the NMR chemical shift of molecules adsorbed on porous carbons. *J. Phys. Chem. C* **118**, 7508–7514 (2014).
- Cervini, L. et al. Factors affecting the nucleus-independent chemical shift in NMR studies of microporous carbon electrode materials. *Energy Storage Mater.* **21**, 335–346 (2019).
- Matsunaga, T., Kubota, T., Sugimoto, T. & Satoh, M. High-performance lithium secondary batteries using cathode active materials of triquinoxalinylenes exhibiting six electron migration. *Chem. Lett.* **40**, 750–752 (2011).
- Hauptler, B., Wild, A. & Schubert, U. S. Carbonyls: powerful organic materials for secondary batteries. *Adv. Energy Mater.* **5**, 1402034 (2015).
- Hollas, A. et al. A biomimetic high-capacity phenazine-based anolyte for aqueous organic redox flow batteries. *Nat. Energy* **3**, 508–514 (2018).
- Conway, B. E. Transition from “supercapacitor” to “battery” behavior in electrochemical energy storage. *J. Electrochem. Soc.* **138**, 1539 (1991).
- Augustyn, V. et al. High-rate electrochemical energy storage through Li⁺ intercalation pseudocapacitance. *Nat. Mater.* **12**, 518–522 (2013).
- Forghani, M. & Donne, S. W. Method comparison for deconvoluting capacitive and pseudo-capacitive contributions to electrochemical capacitor electrode behavior. *J. Electrochem. Soc.* **165**, A664–A673 (2018).
- Ardizzone, S., Fregonara, G. & Trasatti, S. “Inner” and “outer” active surface of RuO₂ electrodes. *Electrochim. Acta* **35**, 263–267 (1990).
- Baronetto, D., Krstajić, N. & Trasatti, S. Reply to “note on a method to interrelate inner and outer electrode areas” by H. Vogt. *Electrochim. Acta* **39**, 2359–2362 (1994).
- Lee, J.-S. M., Briggs, M. E., Hu, C.-C. & Cooper, A. I. Controlling electric double-layer capacitance and pseudocapacitance in heteroatom-doped carbons derived from hypercrosslinked microporous polymers. *Nano Energy* **46**, 277–289 (2018).
- Li, X.-C. et al. Redox-active triazatruxene-based conjugated microporous polymers for high-performance supercapacitors. *Chem. Sci.* **8**, 2959–2965 (2017).
- Lu, Q., Chen, J. G. & Xiao, J. Q. Nanostructured electrodes for high-performance pseudocapacitors. *Angew. Chem. Int. Ed.* **52**, 1882–1889 (2013).
- Xu, J. et al. Facile synthesis of novel metal-organic nickel hydroxide nanorods for high performance supercapacitor. *Electrochim. Acta* **211**, 595–602 (2016).
- McKeown, N. B. et al. Polymers of intrinsic microporosity (PIMs): bridging the void between microporous and polymeric materials. *Chem. Eur. J.* **11**, 2610–2620 (2005).
- Acharya, S. et al. Ultrahigh stability of high-power nanofibrillar PEDOT supercapacitors. *Sustain. Energy Fuels* **1**, 482–491 (2017).
- Witomska, S. et al. Graphene oxide hybrid with sulfur–nitrogen polymer for high-performance pseudocapacitors. *J. Am. Chem. Soc.* **141**, 482–487 (2018).
- Hou, Z., Yang, Q., Lu, H. & Li, Y. Towards enhanced electrochemical capacitance with self-assembled synthesis of poly(pyrrole-co-o-toluidine) nanoparticles. *J. Appl. Polym. Sci.* **133**, 42995 (2016).
- Kim, S. K., Kim, Y. K., Lee, H., Lee, S. B. & Park, H. S. Superior pseudocapacitive behavior of confined lignin nanocrystals for renewable energy-storage materials. *ChemSusChem* **7**, 1094–1101 (2014).
- Park, S. K. et al. 10³ cyclable pseudocapacitive Na-ion storage of hierarchically structured phosphorus-incorporating nanoporous carbons in organic electrolytes. *ACS Energy Lett.* **3**, 724–732 (2018).
- Feng, D. et al. Robust and conductive two-dimensional metal–organic frameworks with exceptionally high volumetric and areal capacitance. *Nat. Energy* **3**, 30–36 (2018).

Publisher's note Springer Nature remains neutral with regard to jurisdictional claims in published maps and institutional affiliations.

© The Author(s), under exclusive licence to Springer Nature Limited 2021

Methods

Synthetic details. All reactions were carried out under an inert atmosphere using standard Schlenk techniques, unless otherwise noted. Dry and deoxygenated solvents were prepared by elution through a dual-column solvent system (Glass Contour).

1-Bromoperylene-3,4,9,10-tetracarboxylic diimide and a mixture of 1,6- and 1,7-dibromoperylene-3,4,9,10-tetracarboxylic diimide were synthesized according to reported procedures³⁷. Tribromo hexaazatrinaphthylene (HATN-Br) was prepared according to a reported procedure³⁸ and used in the synthesis of hexaazatrinaphthylene tris-boronic acid pinacol ester (HATN-bpin). PA-bpin^{39,40} was prepared according to the reported procedures and used in the synthesis of PA-PDI. [1,1'-Bis(diphenylphosphino)ferrocene]dichloropalladium(II) (Pd(dppf)Cl₂), potassium carbonate, cyclohexanone octahydrate, 4-bromobenzene-1,2-diamine and bis(pinacolato)diboron were purchased from Millipore Sigma.

The flow reactor is a home-built reactor^{12,41,42} consisting of a peristaltic pump (Masterflex L/S PTFE-Tubing Pump System; 3–300 r.p.m., 90–260 V_{a.c.}), fluoropolymer tubing (Chemfluor FEP) and 17,500 lumen light-emitting diode corn bulb lamps (EW-IP64CB-150W-E39NB24, 150 W; EverWatt). The tubing was wrapped around the light-emitting diode bulbs to provide the reaction surface. During the photocyclization reaction, the temperature was ~55–65 °C.

Synthesis of HATN-bpin. A 100 ml oven-dried flask was charged with a stir bar, a regioisomeric mixture of tribromo hexaazatrinaphthylene (3.58 g, 5.76 mmol), bis(pinacolato)diboron (8.95 g, 35.4 mmol), Pd(dppf)Cl₂ (412 mg, 0.563 mmol) and potassium acetate (3,390 mg, 34.6 mmol). The charged vial was capped with a rubber septum, evacuated and backfilled with N₂. Degassed dioxane (37.9 ml) was syringed into the flask. The mixture was then heated to 90 °C with stirring overnight. The solution was cooled to room temperature and diluted with dichloromethane, then dried. The crude mixture was dissolved in dichloromethane and filtered over a silica plug. This dark green solution was then dried again, brought up in a small amount of dichloromethane and triturated into methanol. The suspension was washed over a Celite plug using methanol and a blue solution was pulled through using dichloromethane. This solution was dried to afford the yellow-green solid HATN-bpin in 73% yield (3.2 g) consisting of a mixture of regioisomers. This regiomiixture was carried forward through the following synthetic steps without further resolution. NMR spectra are provided in Supplementary Figs. 1 and 2.

Synthesis of uncyclized PHATN. A 20 ml vial was charged with a stir bar, HATN-bpin (460 mg, 0.6 mmol), a mixture of 1,6- and 1,7-dibromoperylene-3,4,9,10-tetracarboxylic diimide (770 mg, 0.9 mmol), Pd(dppf)Cl₂ (88 mg, 0.120 mmol) and potassium carbonate (665 mg, 4.8 mmol). The charged vial was capped with a rubber septum, evacuated and backfilled with N₂. Degassed water (1.5 ml) and degassed tetrahydrofuran (6.0 ml) were syringed into the vial. The mixture was then heated to 57 °C with stirring overnight. The solution was cooled to room temperature and diluted with water and dichloromethane. The mixture was triturated with methanol and the solid was collected. The solid was subjected to consecutive Soxhlet extractions comprised of methanol, hexanes and chloroform. The chloroform fraction was collected and dried to yield uncyclized PHATN as a maroon solid in 61% yield (520 mg).

Synthesis of PHATN. In a 100 ml round-bottom flask, uncyclized PHATN (100 mg) and iodine (25 mg) were dissolved in chlorobenzene (65 ml). The mixture was stirred for 15 min and then irradiated for 72 h with visible light using the home-built reactor described above. The solvent was then removed under vacuum and the resulting solid was suspended in methanol and loaded onto a Celite plug. The solid was washed with methanol, hexanes and acetonitrile and then redissolved in chloroform. The solvent was removed under vacuum to afford cyclized PHATN as an orange solid in 90% yield (90 mg). The NMR of the PHATN monomer (Supplementary Fig. 3) was used to assign the conformation of the extended material. Cyclized PHATN (141 mg) was sealed in a borosilicate glass tube under vacuum. The tube was placed in a tube furnace, with one end of the tube sticking out of the furnace and the other end containing the solid in the middle of the furnace. The furnace was heated to 375 °C for 2 h, over which time the material turned black and a clear, yellow liquid condensed at the cool end of the tube. The tube was opened and thermolysed PHATN was collected as an orange-black solid in 63% yield (89 mg).

Synthesis of PHATN monomer.

1. A 3 ml vial was charged with a stir bar, HATN-bpin (92 mg, 0.12 mmol), 1-bromoperylene-3,4,9,10-tetracarboxylic diimide (290 mg, 0.372 mmol), Pd(dppf)Cl₂ (22 mg, 0.03 mmol) and potassium carbonate (133 mg, 0.96 mmol). The vial was capped with a rubber septum, evacuated and backfilled with N₂. Degassed water (0.3 ml) and degassed tetrahydrofuran (1.2 ml) were syringed into the vial. The mixture was then heated to 57 °C with stirring overnight. The solution was cooled to room temperature and diluted with water and dichloromethane. The mixture was triturated with methanol and the solid was collected. The solid was washed with water then

subjected to consecutive Soxhlet extractions comprised of methanol, hexanes and chloroform. The chloroform fraction was collected and dried to afford uncyclized PHATN monomer as a maroon solid in 64% yield (190 mg).

2. In a 100 ml round-bottom flask, uncyclized PHATN monomer (100 mg) and iodine (25 mg) were dissolved in chlorobenzene (65 ml). The mixture was stirred for 15 min and then irradiated for 72 h with visible light using a home-built photoreactor. The solvent was then removed under vacuum and the resulting solid was suspended in methanol and loaded onto a Celite plug. The solid was washed with methanol, hexanes and then redissolved in chloroform. The solvent was removed under vacuum to provide a regioisomeric mixture of PHATN 'monomer' as an orange solid. The symmetric isomer could be isolated in small yield by preparatory thin-layer chromatography methods and was used for structural assignment by NMR (Supplementary Figs. 3 and 4).

Synthesis of uncyclized PA-PDI. A 50 ml vial was charged with a stir bar, PA-dibpin (400 mg, 0.93 mmol), a mixture of 1,6- and 1,7-dibromoperylene-3,4,9,10-tetracarboxylic diimide (720 mg, 0.93 mmol), Pd(dppf)Cl₂ (136 mg, 0.19 mmol) and potassium carbonate (1,020 mg, 7.4 mmol). The charged vial was capped with a rubber septum, evacuated and backfilled with N₂. Degassed water (1.5 ml) and degassed tetrahydrofuran (6.0 ml) were added to the vial with a syringe. The mixture was then heated to 57 °C with stirring overnight. The solution was cooled to room temperature and reduced under vacuum. The mixture was triturated with methanol and the solid was collected. The solid was subjected to consecutive Soxhlet extractions comprised of methanol, hexanes and chloroform. The chloroform fraction was collected and dried to yield uncyclized PA-PDI as a purple-black solid in 83% yield (671 mg).

Synthesis of cyclized PA-PDI. In a 150 ml Erlenmeyer flask, uncyclized PA-PDI (251 mg) and iodine (36 mg) were dissolved in a mixture of chlorobenzene (100 ml) and chloroform (20 ml). The mixture was stirred until completely dissolved then irradiated for 72 h with visible light using the home-built reactor described above. The solvent was then removed under vacuum and the resulting solid was suspended in methanol and isolated using vacuum filtration and washed using methanol. After collecting the solid, any additional solvent was removed under vacuum to afford cyclized PA-PDI as a dark purple solid in 38% yield (96 mg). Cyclized PA-PDI (96 mg) was sealed in a quartz tube under vacuum. The tube was placed in a tube furnace, with one end of the tube sticking out of the furnace and the other end containing the solid in the middle of the furnace. The furnace was heated to 375 °C for 2 h, over which time the material turned black and a clear, yellow liquid condensed at the cool end of the tube. The tube was opened and thermolysed PA-PDI was collected as a purple-black solid in 60% yield (58 mg).

NMR. ¹H spectra were recorded using a Bruker AVANCE III 500 (500 MHz) spectrometer, and ¹³C spectra were recorded using a Bruker AVANCE III 400SL (400 MHz) spectrometer. Chemical shifts for protons are reported in parts per million downfield from tetramethylsilane and are referenced to residual protium within the NMR solvent (CDCl₃: δ 7.26 or C₂D₂Cl₂: δ 6.00).

Solid-state NMR. The ssNMR experiments were performed using a Bruker Avance NEO 600 MHz spectrometer equipped with a 1.6 mm HXY MAS (magic-angle spinning) Chemagnetics probehead operating at 599.37 MHz for ¹H and 150.71 MHz for ¹³C. Samples were packed in 1.6 mm ZrO₂ rotors and sealed with Torlon caps for measurement. Before each set of experiments, the magic angle was set using KBr. ¹H–¹³C cross polarization-MAS measurements were performed with a Hartmann–Hahn match of 60 kHz with a ramped (90–100%) pulse on ¹H, a contact time of 3 ms, a recycle delay of 3 s, ¹H decoupling at 120 kHz using two-pulse phase modulation and with between 4,000 and 27,000 scans (depending on the sample). ¹H NMR was externally referenced to adamantane at 1.85 ppm; ¹³C NMR was referenced to adamantane at 38.5 ppm.

Thermogravimetric analysis. Thermogravimetric analysis traces were collected using a TA Instruments Q500 analyser under nitrogen flow.

Infrared spectroscopy. Infrared spectra were collected using a Perkin Elmer Spectrum 400 FT-IR instrument.

Gas adsorption measurements. Gas adsorption isotherms for pressures in the range of 0–760 torr were measured by a volumetric method using a Micromeritics ASAP 2020 gas sorption analyser. Measurements were collected on approximately 200 mg of sample, which was evacuated by heating at 150 °C with a ramp rate of 10 °C min⁻¹ under dynamic vacuum for 3 h. Free-space correction measurements were performed using ultrahigh purity He gas. Ultrahigh purity (99.999%) CO₂ was used for measurements. Isotherms of CO₂ collected at 195 K were measured in a dry ice/isopropanol bath. Oil-free vacuum pumps and oil-free pressure regulators were used for all measurements to prevent contamination of the samples during the evacuation process, or of the feed gases during the isotherm measurements.

Gas chromatography-mass spectrometry. Gas chromatography-mass spectrometry data were collected using an Agilent Technologies GC-MS

instrument consisting of a 7890B GC inlet, 5977B mass spectrometer (electron impact ionization, EI) and a PAL LSI 85 autosampler.

Powder X-ray diffraction. Powder X-ray diffraction patterns were measured using a PANalytical XPert3 Powder X-ray diffractometer, on a rotating Si zero-background plate.

Electrochemical characterization. Electrochemical measurements, including CV, GCD and EIS, were performed using a Bio-Logic VSP-300 potentiostat/galvanostat running EC-lab software.

Solution-phase CV. The molecule of interest (PDI, HATN-Br or the PHATN monomer) was dissolved to a known concentration (0.01, 0.001 or 0.005 M, respectively) in a solution of dichloromethane with 0.1 M tetrabutylammonium hexafluorophosphate as the supporting electrolyte. A three-electrode setup was used with a 3 mm glassy-carbon disc or a 1.6 mm platinum disc as the working electrode, platinum wire as the counter electrode and a non-aqueous reference electrode composed of 0.01 M Ag/AgNO₃ in acetonitrile. Measurements were performed in a glovebox under N₂ atmosphere. The potential was swept from open-circuit voltage to -1.7 V at rates ranging from 10 to 200 mV s⁻¹.

No difference was observed between the glassy-carbon and platinum working electrodes after correcting for the electrode area. The glassy-carbon electrode was used for subsequent measurements.

The peak current (i) from the cathodic trace of each scan was plotted versus the square root of the sweep rate (v ; Supplementary Fig. 9). The resulting linear shape for each molecule indicates that each diffuses freely in solution without adsorption to the electrode, according to the Randles–Sevcik equation:

$$i = 0.446nFAC^0 \sqrt{\frac{nFvD_0}{RT}}$$

where n is the number of electrons transferred, F is Faraday's constant, A is the surface area of the electrode, C^0 is the molecule concentration and D_0 is the diffusion coefficient of the reduced molecule.

Electrode fabrication. The active material was ground using an agate mortar and pestle. The material was combined with carbon black and PTFE (60% w/w suspension in water) in a mass ratio of 80:10:10, respectively. Approximately 3.6 times the total mass of the mixture was then added of *N*-methyl-2-pyrrolidone to form a slurry. The slurry was stirred for several hours. Carbon paper (AvCarb MGL190) was cut into rectangles (~ 0.5 – 1 cm \times 1 – 2 cm) and the resulting substrates were sonicated in 1 M H₂SO₄ for 20 min to remove any residue or carbon dust. The substrates were then washed with deionized water and acetone, dried at 60 °C under vacuum and weighed on an analytical balance (0.001 mg precision). The slurry was manually deposited on the bottom half of the substrates and pressed using a spatula. The electrode was dried at 70 °C under vacuum overnight. The electrode was then weighed on an analytical balance to obtain the active material mass. Typically, the mass loading was 2–3 mg cm⁻². Finally, before testing, the electrode was soaked in 6 M aqueous KOH solution under static vacuum for several hours.

Three-electrode measurements. Unless otherwise noted, measurements were performed in 6 M aqueous KOH electrolyte prepared from ultra-pure distilled water. Compared with organic electrolytes, the aqueous electrolyte has a higher conductivity and may provide a lower viscosity for faster ion diffusion through the material. Measurements were performed in a three-electrode cell with ~ 20 ml of electrolyte. A copper clip was used to hold the carbon paper working electrode, with a small piece of titanium foil interposed to prevent contact with the electrolyte. The counter electrode was a graphite rod and the reference was a Hg/HgO reference electrode in 6 M KOH (BASi). Before measurement the electrolyte was sparged for 10 min with N₂ and the cell was subsequently kept under a blanketing N₂ atmosphere.

CV experiments were performed in the range of -1.25 to -0.3 V versus Hg/HgO, at rates from 1 to 300 mV s⁻¹. GSD measurements were performed by applying a constant current, with the current switching signs upon reaching set voltage limits of -1.15 and -0.65 V. The set current density was calculated using the equation:

$$I = \frac{i}{m_a}$$

where I is the current density, ranging from 0.5 to 75 A g⁻¹, i is the current and m_a is the mass of active material. Unless stated otherwise, potentiostatic EIS measurements were performed at -0.7 V versus Hg/HgO in the frequency range of 100 kHz to 20 mHz with a sinus amplitude of 5 mV.

Peak current potentials for the cathodic shift (Fig. 3a) and i - v plots (Fig. 3b) were found with the EC-lab peak finding function and were taken from the first reduction peak (approximately -0.7 V). Capacity values for the capacity versus rate plots (Fig. 3c,d) were found by integrating under the CV curve.

Calculation of specific and volumetric capacitance. Specific capacitance via GCD.

$$C_s = \frac{i \times t}{m_a \times \Delta E}$$

where i is the current, t is the cycle time, m_a is the measured mass of the active material and ΔE is the change in potential between the voltage limits.

Via EIS, series model.

$$C_s = \frac{-1}{Z'' \times 2\pi \times f}$$

where Z'' is the imaginary component of the resistance and f is the EIS frequency.

Volumetric capacitance. PHATN (30 mg) was pressed into a circular pellet under 4 tons of pressure and measured (1.1 mm thick, 5 mm diameter). The resulting volume (21.6 mm³) was used to calculate the density of PHATN (1.39 g cm⁻³). This density multiplied by specific capacitance gives the volumetric capacitance.

Potential-dependent EIS. The potential was held for 1 min. Then, a sinusoidal potential was applied with 5 mV amplitude and frequencies ranging from 100 kHz to 20 mHz.

Characterization in organic electrolyte. The supporting electrolyte was 0.1 M tetraethylammonium hexafluorophosphate (TEA-PF₆), the counter electrode was a platinum mesh and the non-aqueous reference electrode was 0.01 M AgNO₃ in acetonitrile. Measurements were performed in a glovebox under N₂ atmosphere.

Diffusion coefficient. The chemical diffusion coefficient, D , can be estimated from the GITT data using the equation⁴³

$$D = \frac{4}{\pi \times \tau} \times \left(\frac{m \times \rho}{S} \right)^2 \times \left(\frac{\Delta V_s}{\Delta V_T} \right)^2$$

where τ is the current pulse length, m is the mass of the active material on the electrode, ρ is the density of the active material, S is the surface area of the electrode, ΔV_s is the change in steady-state potential after each current pulse and ΔV_T is the change in potential during the current pulse.

Two-electrode measurements. Two-electrode cells consisted of one PHATN electrode and one counter electrode, assembled into one of three different cell types: a button cell, a small pouch cell and a large pouch cell. The PHATN electrodes were fabricated as described above, using carbon paper (AvCarb MGL190) as the current collector.

Counter-electrode fabrication. Two types of counter electrodes were fabricated:

1. AC counter electrode: the AC was prepared using the alkali activation method⁴⁴. Briefly, an apricot pit produced from north China was used as the starting material. The apricot pit was heated to 550 °C and pyrolysed for 1 h in a tubular furnace under nitrogen (99.999%). The resulting char and KOH were mixed with a weight ratio of 1:2 and heated to 700 °C under nitrogen for 2 h to activate the material. After activation, the product was sequentially washed with 0.5 M HCl, hot water and distilled water to remove the residual base completely, followed by drying at 120 °C for 12 h to obtain the final AC sample. A mixture of 87 wt% AC, 10 wt% of acetylene black (Jinpu) and 3 wt% of PTFE binder (Shanghai Macklin) was prepared and hot pressed into sheets with a thickness of ~ 0.35 mm as supercapacitor electrodes. The mass loading was 11 mg cm⁻².
2. Ni(OH)₂ counter electrode: the Ni(OH)₂ electrode was extracted from a discharged commercial nickel metal hydride battery and cut into a 1 \times 1 cm square. The material was scraped off one face of the electrode. The mass loading (wet) of Ni(OH)₂ was around 100 mg cm⁻².

Button-cell assembly. Two-electrode button cells were assembled according to established protocols⁴⁵. Briefly, a circular PHATN electrode (1.27 cm diameter) was fabricated as described above. The mass loading was 6.4 mg cm⁻². This electrode was stacked with a cellulose filter paper separator (Whatman Grade 1, thickness = 180 μ m) and an a.c. electrode (1.27 cm diameter, fabrication as described above) and wetted with 250 μ l of 6 M KOH aqueous electrolyte (31 μ l mg⁻¹ active material). A steel spacer and spring were then added and the stack was enclosed in a steel button-cell shell and sealed with Parafilm to prevent electrolyte evaporation. The cell was then tested using a standard spring-loaded clip connected to the potentiostat (see Supplementary Fig. 13).

Small pouch-cell assembly. Square electrodes with 1 cm² area were prepared as described above, with ~ 2 mg cm⁻² mass loading of PHATN. AC (see above) was used as the counter electrode. The two electrodes were separated with a cellulose filter paper separator (Whatman Grade 1, thickness = 180 μ m) and wetted with

300 μl of 6 M KOH aqueous electrolyte. The stack was placed inside a plastic pouch ($\sim 5 \times 5$ cm), contacted with titanium foil strips as the current collectors (thickness ~ 0.13 mm) and sealed using an impulse heat sealer. No pressure or calendaring was applied during sealing. The cell was clamped in a vice with flat blocks on either side to ensure good contact between all components, under a pressure of ~ 100 pounds per square inch. The cell was then connected to the potentiostat (see Supplementary Fig. 16).

Large pouch-cell assembly. Square electrodes of 10 cm^2 area were prepared with a 6.7 mg cm^{-2} mass loading of PHATN. AC (see above) was used as the counter electrode. The two electrodes were separated with a cellulose filter paper separator (Whatman Grade 1, thickness = $180\text{ }\mu\text{m}$) and wetted with $750\text{ }\mu\text{l}$ of 6 M KOH aqueous electrolyte ($11\text{ }\mu\text{l mg}^{-1}$ active material). The stack was placed inside a plastic pouch ($\sim 4 \times 4$ cm), contacted with titanium foil strips as the current collectors (thickness ~ 0.13 mm) and sealed under vacuum using a vacuum heat sealer. The cell was clamped in a vice with flat blocks on either side to ensure good contact between all components, under a pressure of ~ 100 pounds per square inch. The cell was then connected to the potentiostat (see Supplementary Fig. 21).

Calculation of specific capacity, energy and power. The specific capacity, energy and power for the two-electrode cells were calculated from GCD data (discharge cycle). The specific capacity is calculated using the equation

$$Q_s = \frac{i \times t}{m_a}$$

where i is the current, t is the cycle time and m_a is the mass of active material (PHATN) on the anode.

For calculating the specific energy and power of the two-electrode cell, we use the total mass of all cell components, as is typical in the literature^{46,47}. The specific energy is calculated using the equation

$$E_s = \frac{i \times t \times \Delta E}{m_{\text{total}}}$$

where ΔE is the change in potential and m_{total} is given by

$$m_{\text{total}} = m_a + m_c + m_e$$

where m_c is the theoretical mass of $\text{Ni}(\text{OH})_2$ or AC required to balance the measured discharge Q or C , respectively. For $\text{Ni}(\text{OH})_2$ this is based on the theoretical capacity of $\text{Ni}(\text{OH})_2$ (289.04 mAh g^{-1}), whereas for AC this is based on the reported capacitance of the AC material used (339 F g^{-1})⁴⁴. The parameter m_e is the theoretical mass of electrolyte required to supply ions for the measured discharge Q .

The specific power was calculated using the equation

$$P_s = \frac{i \times \Delta E}{m_{\text{total}}}$$

Computational modelling. Quantum chemical calculations were performed using Jaguar 8.7 (Schrödinger)⁴⁸. Geometries were optimized using the B3LYP or M06-2X functional and the 6-31G** basis set. The geometry of the PHATN monomer is presented in Extended Data Fig. 2 as a rough electronic approximation of the geometry of the extended material PHATN.

Data availability

The data that support the findings of this study are available from the corresponding authors upon reasonable request.

References

- Rajasingh, P., Cohen, R., Shirman, E., Shimon, L. J. & Rybtchinski, B. Selective bromination of perylene diimides under mild conditions. *J. Org. Chem.* **72**, 5973–5979 (2007).
- Wang, J., Lee, Y., Tee, K., Riduan, S. N. & Zhang, Y. A nanoporous sulfur-bridged hexaazatrinaphthylene framework as an organic cathode for lithium ion batteries with well-balanced electrochemical performance. *Chem. Commun.* **54**, 7681–7684 (2018).
- Yu, W. et al. Discovery of fused tricyclic core containing HCV NS5A inhibitors with pan-genotype activity. *Bioorg. Med. Chem. Lett.* **26**, 3158–3162 (2016).
- Vitaku, E. et al. Phenazine-based covalent organic framework cathode materials with high energy and power densities. *J. Am. Chem. Soc.* **142**, 16–20 (2019).
- Sisto, T. J. et al. Long, atomically precise donor–acceptor cove-edge nanoribbons as electron acceptors. *J. Am. Chem. Soc.* **139**, 5648–5651 (2017).
- Peurifoy, S. R. et al. Designing three-dimensional architectures for high-performance electron accepting pseudocapacitors. *J. Am. Chem. Soc.* **140**, 10960–10964 (2018).
- Shen, Z., Cao, L., Rahn, C. D. & Wang, C.-Y. Least squares galvanostatic intermittent titration technique (LS-GITT) for accurate solid phase diffusivity measurement. *J. Electrochem. Soc.* **160**, A1842 (2013).
- Xu, B. et al. Activated carbon with high capacitance prepared by NaOH activation for supercapacitors. *Mater. Chem. Phys.* **124**, 504–509 (2010).
- Muench, S. et al. Polymer-based organic batteries. *Chem. Rev.* **116**, 9438–9484 (2016).
- Li, H. et al. A high-performance sodium-ion hybrid capacitor constructed by metal–organic framework–derived anode and cathode materials. *Adv. Energy Mater.* **28**, 1800757 (2018).
- Zheng, J. P. The limitations of energy density of battery/double-layer capacitor asymmetric cells. *J. Electrochem. Soc.* **150**, A484 (2003).
- Bochevarov, A. D. et al. Jaguar: a high-performance quantum chemistry software program with strengths in life and materials sciences. *Int. J. Quantum Chem.* **113**, 2110–2142 (2013).
- Lee, S. W. et al. High-power lithium batteries from functionalized carbon-nanotube electrodes. *Nat. Nanotechnol.* **5**, 531–537 (2010).
- Zeng, L. et al. Carbonaceous mudstone and lignin-derived activated carbon and its application for supercapacitor electrode. *Surf. Coat. Technol.* **357**, 580–586 (2019).
- Su, X.-L. et al. Three-dimensional porous activated carbon derived from loofah sponge biomass for supercapacitor applications. *Appl. Surf. Sci.* **436**, 327–336 (2018).
- Wang, Y., Tao, S., An, Y., Wu, S. & Meng, C. Bio-inspired high performance electrochemical supercapacitors based on conducting polymer modified coral-like monolithic carbon. *J. Mater. Chem. A* **1**, 8876–8887 (2013).
- Kim, M., Lee, C. & Jang, J. Fabrication of highly flexible, scalable, and high-performance supercapacitors using polyaniline/reduced graphene oxide film with enhanced electrical conductivity and crystallinity. *Adv. Funct. Mater.* **24**, 2489–2499 (2014).
- Milczarek, G. & Inganäs, O. Renewable cathode materials from biopolymer/conjugated polymer interpenetrating networks. *Science* **335**, 1468–1471 (2012).
- Bachman, J. C. et al. Electrochemical polymerization of pyrene derivatives on functionalized carbon nanotubes for pseudocapacitive electrodes. *Nat. Commun.* **6**, 7040 (2015).
- Li, M. & Yang, L. Intrinsic flexible polypyrrole film with excellent electrochemical performance. *J. Mater. Sci. Mater. Electron.* **26**, 4875–4879 (2015).
- Grover, S. et al. Polyaniline all solid-state pseudocapacitor: role of morphological variations in performance evolution. *Electrochim. Acta* **196**, 131–139 (2016).
- Su, D., Zhang, J., Dou, S. & Wang, G. Polypyrrole hollow nanospheres: stable cathode materials for sodium-ion batteries. *Chem. Commun.* **51**, 16092–16095 (2015).
- Cong, H.-P., Ren, X.-C., Wang, P. & Yu, S.-H. Flexible graphene–polyaniline composite paper for high-performance supercapacitor. *Energy Environ. Sci.* **6**, 1185–1191 (2013).
- Cai, Z. et al. Flexible, weavable and efficient microsupercapacitor wires based on polyaniline composite fibers incorporated with aligned carbon nanotubes. *J. Mater. Chem. A* **1**, 258–261 (2013).
- Shen, K. et al. Supercapacitor electrodes based on nano-polyaniline deposited on hollow carbon spheres derived from cross-linked co-polymers. *Synth. Met.* **209**, 369–376 (2015).
- Wang, S. et al. Free-standing 3D graphene/polyaniline composite film electrodes for high-performance supercapacitors. *J. Power Sources* **299**, 347–355 (2015).
- Sun, H. et al. A self-standing nanocomposite foam of polyaniline@reduced graphene oxide for flexible super-capacitors. *Synth. Met.* **209**, 68–73 (2015).
- Wang, Z., Tammela, P., Zhang, P., Strömme, M. & Nyholm, L. High areal and volumetric capacity sustainable all-polymer paper-based supercapacitors. *J. Mater. Chem. A* **2**, 16761–16769 (2014).
- Seok, J. Y., Lee, J. & Yang, M. Self-generated nanoporous silver framework for high-performance iron oxide pseudocapacitor anodes. *ACS Appl. Mater. Interfaces* **10**, 17223–17231 (2018).
- Pan, Z. et al. In situ growth of layered bimetallic ZnCo hydroxide nanosheets for high-performance all-solid-state pseudocapacitor. *ACS Nano* **12**, 2968–2979 (2018).
- Pang, H. et al. Cu superstructures fabricated using tree leaves and Cu–MnO₂ superstructures for high performance supercapacitors. *J. Mater. Chem. A* **1**, 5053–5060 (2013).
- Ding, K., Zhang, X., Li, J., Yang, P. & Cheng, X. Phase and morphology evolution of ultrathin Co(OH)₂ nanosheets towards supercapacitor application. *CrystEngComm* **19**, 5780–5786 (2017).
- Song, Y. et al. A polyanionic molybdenophosphate anode for a 2.7 V aqueous pseudocapacitor. *Nano Energy* **65**, 104010 (2019).
- Chen, H. et al. One-step fabrication of ultrathin porous nickel hydroxide–manganese dioxide hybrid nanosheets for supercapacitor electrodes with excellent capacitive performance. *Adv. Energy Mater.* **3**, 1636–1646 (2013).

71. Qiu, K. et al. Mesoporous, hierarchical core/shell structured ZnCo₂O₄/MnO₂ nanocone forests for high-performance supercapacitors. *Nano Energy* **11**, 687–696 (2015).
72. Wu, M.-S. & Wu, J.-F. Nickel hydroxide electrode with porous nanotube arrays prepared by hydrolysis and cathodic deposition for high-performance supercapacitors. *J. Power Sources* **240**, 397–403 (2013).
73. Soltanloo, M., Kazazi, M., Yeganeh, S. E. H., Chermahini, M. D. & Mazinani, B. High-performance pseudocapacitive electrode based on electrochemically deposited NiCo₂O₄/MWCNTs nanocomposite on 316L stainless steel. *JOM* **72**, 2235–2244 (2020).
74. Liu, X. et al. Multi-shelled Ni₆MnO₈ hollow microspheres for high-performance supercapacitors. *Mater. Res. Express* **7**, 065502 (2020).
75. Yang, G.-W., Xu, C.-L. & Li, H.-L. Electrodeposited nickel hydroxide on nickel foam with ultrahigh capacitance. *Chem. Commun.* <https://doi.org/10.1039/B815647F> (2008).
76. Gupta, A. K., Saraf, M., Bharadwaj, P. K. & Mobin, S. M. Dual functionalized CuMOF-based composite for high-performance supercapacitors. *Inorg. Chem.* **58**, 9844–9854 (2019).
77. Chen, G.-F., Liu, Z.-Q., Lin, J.-M., Li, N. & Su, Y.-Z. Hierarchical polypyrrole based composites for high performance asymmetric supercapacitors. *J. Power Sources* **283**, 484–493 (2015).
78. Jagadale, A. D. et al. Cobalt hydroxide [Co(OH)₂] loaded carbon fiber flexible electrode for high performance supercapacitor. *RSC Adv.* **5**, 56942–56948 (2015).
79. Wang, H., Casalongue, H. S., Liang, Y. & Dai, H. Ni(OH)₂ nanoplates grown on graphene as advanced electrochemical pseudocapacitor materials. *J. Am. Chem. Soc.* **132**, 7472–7477 (2010).
80. Li, L., Chen, L., Qian, W., Xie, F. & Dong, C. Directly grown multiwall carbon nanotube and hydrothermal MnO₂ composite for high-performance supercapacitor electrodes. *Nanomaterials* **9**, 703 (2019).
81. Zhang, F. et al. A high-performance supercapacitor-battery hybrid energy storage device based on graphene-enhanced electrode materials with ultrahigh energy density. *Energy Environ. Sci.* **6**, 1623–1632 (2013).
82. Ma, H. et al. Disassembly–reassembly approach to RuO₂/graphene composites for ultrahigh volumetric capacitance supercapacitor. *Small* **13**, 1701026 (2017).
83. Wang, Y. et al. Ultrathin NiCo-MOF nanosheets for high-performance supercapacitor electrodes. *ACS Appl. Energy Mater.* **2**, 2063–2071 (2019).
84. Zhai, T. et al. Phosphate ion functionalized Co₃O₄ ultrathin nanosheets with greatly improved surface reactivity for high performance pseudocapacitors. *Adv. Mater.* **29**, 1604167 (2017).
85. Sun, X. et al. Fabrication of PANI-coated honeycomb-like MnO₂ nanospheres with enhanced electrochemical performance for energy storage. *Electrochim. Acta* **180**, 977–982 (2015).
86. Sun, M. et al. In situ growth of burl-like nickel cobalt sulfide on carbon fibers as high-performance supercapacitors. *J. Mater. Chem. A* **3**, 1730–1736 (2015).
87. Zhou, J. et al. Importance of polypyrrole in constructing 3D hierarchical carbon nanotube@MnO₂ perfect core–shell nanostructures for high-performance flexible supercapacitors. *Nanoscale* **7**, 14697–14706 (2015).
88. Zhang, X., Ji, L., Zhang, S. & Yang, W. Synthesis of a novel polyaniline-intercalated layered manganese oxide nanocomposite as electrode material for electrochemical capacitor. *J. Power Sources* **173**, 1017–1023 (2007).
89. Li, L. et al. Facile Synthesis of MnO₂/CNTs composite for supercapacitor electrodes with long cycle stability. *J. Phys. Chem. C* **118**, 22865–22872 (2014).
90. Liu, Z., Xu, K., Sun, H. & Yin, S. One-step synthesis of single-layer MnO₂ nanosheets with multi-role sodium dodecyl sulfate for high-performance pseudocapacitors. *Small* **11**, 2182–2191 (2015).
91. Liang, Y. et al. Direct access to metal or metal oxide nanocrystals integrated with one-dimensional nanoporous carbons for electrochemical energy storage. *J. Am. Chem. Soc.* **132**, 15030–15037 (2010).
92. Rajagopal, R., Lee, Y. S. & Ryu, K.-S. Synthesis and electrochemical analysis of Nb₂O₅-TiO₂/H-rGO sandwich type layered architecture electrode for supercapacitor application. *Chem. Eng. J.* **325**, 611–623 (2017).
93. Mathis, T. S. et al. Energy storage data reporting in perspective—guidelines for interpreting the performance of electrochemical energy storage systems. *Adv. Energy Mater.* **9**, 1902007 (2019).
94. Yeager, H. & Steck, A. Cation and water diffusion in Nafion ion exchange membranes: influence of polymer structure. *J. Electrochem. Soc.* **128**, 1880 (1981).
95. Splith, T., Fröhlich, D., Henninger, S. K. & Stallmach, F. Development and application of an exchange model for anisotropic water diffusion in the microporous MOF aluminum fumarate. *J. Magn. Reson.* **291**, 40–46 (2018).

Acknowledgements

This work was supported by the US National Science Foundation Division of Materials Research under Award number DMR-2002634 and the Office of Naval Research (ONR) under Award no. N00014-16-1-2921. The electrochemical measurement apparatus was purchased with the help of the US Air Force Office of Scientific Research (AFOSR) Grant No. FA9550-18-1-0020. C.N. thanks S. Buckler and D. Buckler for their generous support. J.C.R. and S.R.P. are supported by the US Department of Defense through the National Defense Science & Engineering Graduate Fellowship (NDSEG) Program. V.A.P. is supported by the National Science Foundation Graduate Research Fellowship Program (NSF GRFP #2019279091). D.A.R. thanks the Columbia Nano Initiative for postdoctoral fellowship support. L.E.M. thanks Columbia University for lab startup funding. Y.Y. acknowledges support from the Air Force Office of Scientific Research (FA9550-20-1-0233).

Author contributions

J.C.R., Y.Y., X.R., C.N. and S.R.P. designed the experiments. S.R.P. and J.G. synthesized and spectroscopically characterized the materials. J.C.R. and V.A.P. fabricated the devices and performed the electrochemical measurements. R.M. and L.E.M. performed solid-state NMR measurements. D.A.R. and S.R.P. performed the gas adsorption analysis. H.Z. provided the activated carbon electrodes. S.R.P. and M.L.S. performed the DFT modelling. All authors discussed the data and contributed to writing the manuscript.

Competing interests

The authors declare no competing interests.

Additional information

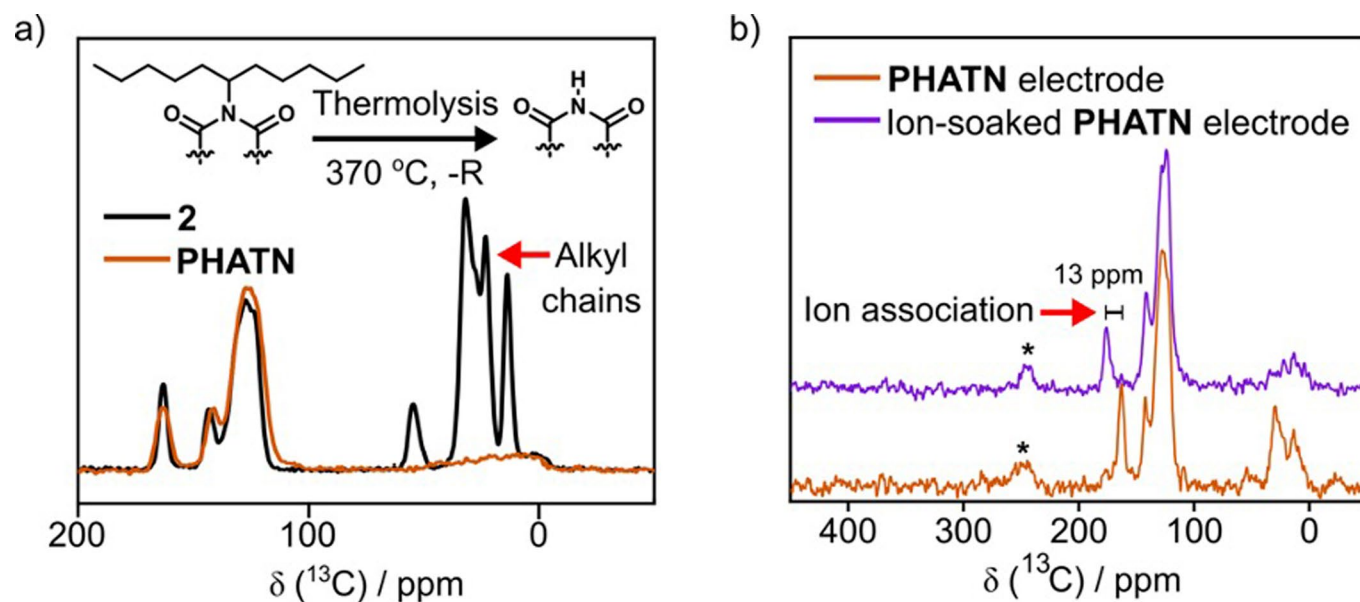
Extended data is available for this paper at <https://doi.org/10.1038/s41563-021-00954-z>.

Supplementary information The online version contains supplementary material available at <https://doi.org/10.1038/s41563-021-00954-z>.

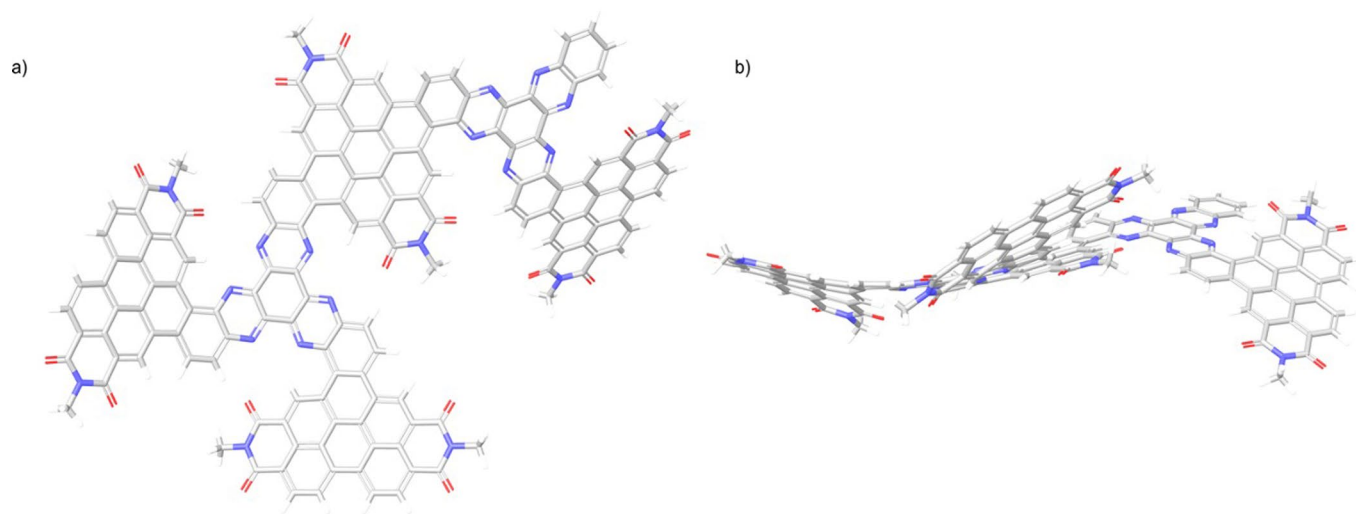
Correspondence and requests for materials should be addressed to X.R., C.N. or S.R.P.

Peer review information *Nature Materials* thanks Olivier Fontaine and the other, anonymous, reviewer(s) for their contribution to the peer review of this work.

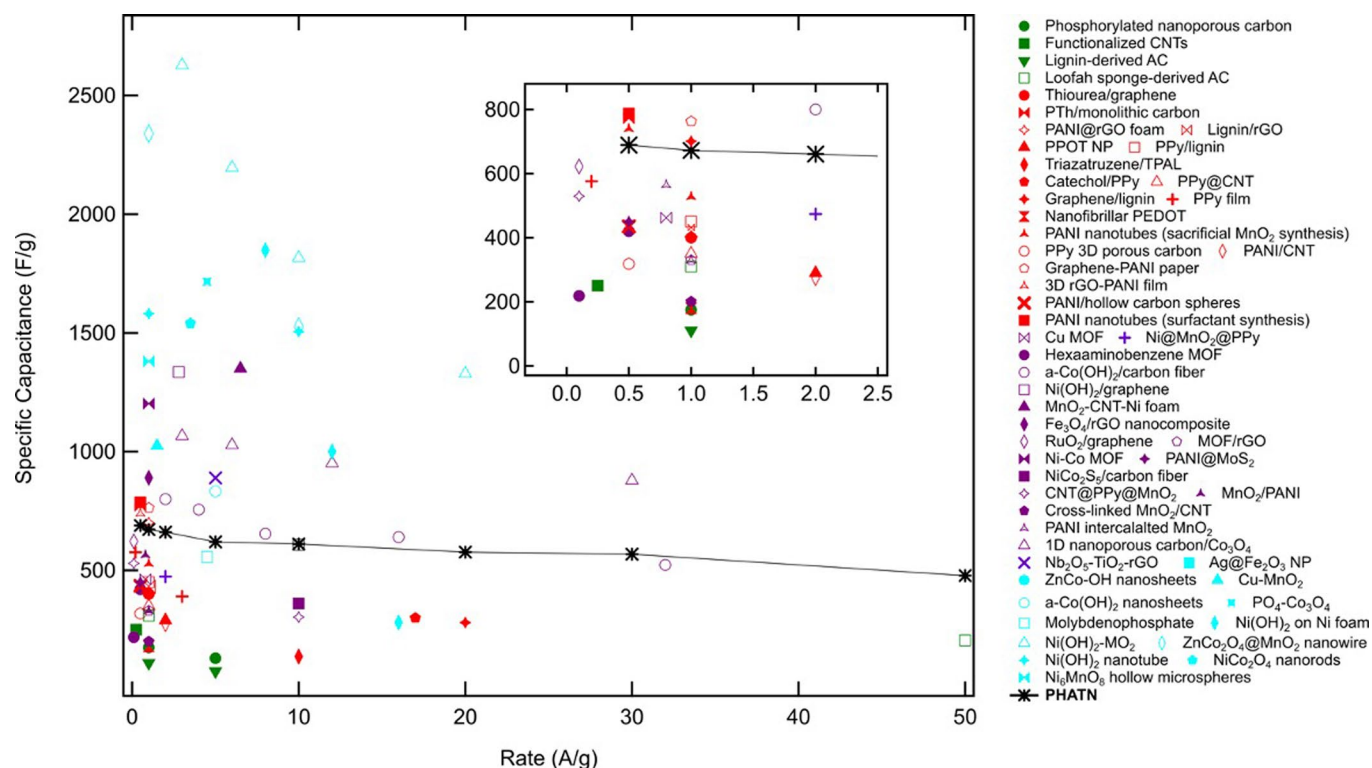
Reprints and permissions information is available at www.nature.com/reprints.



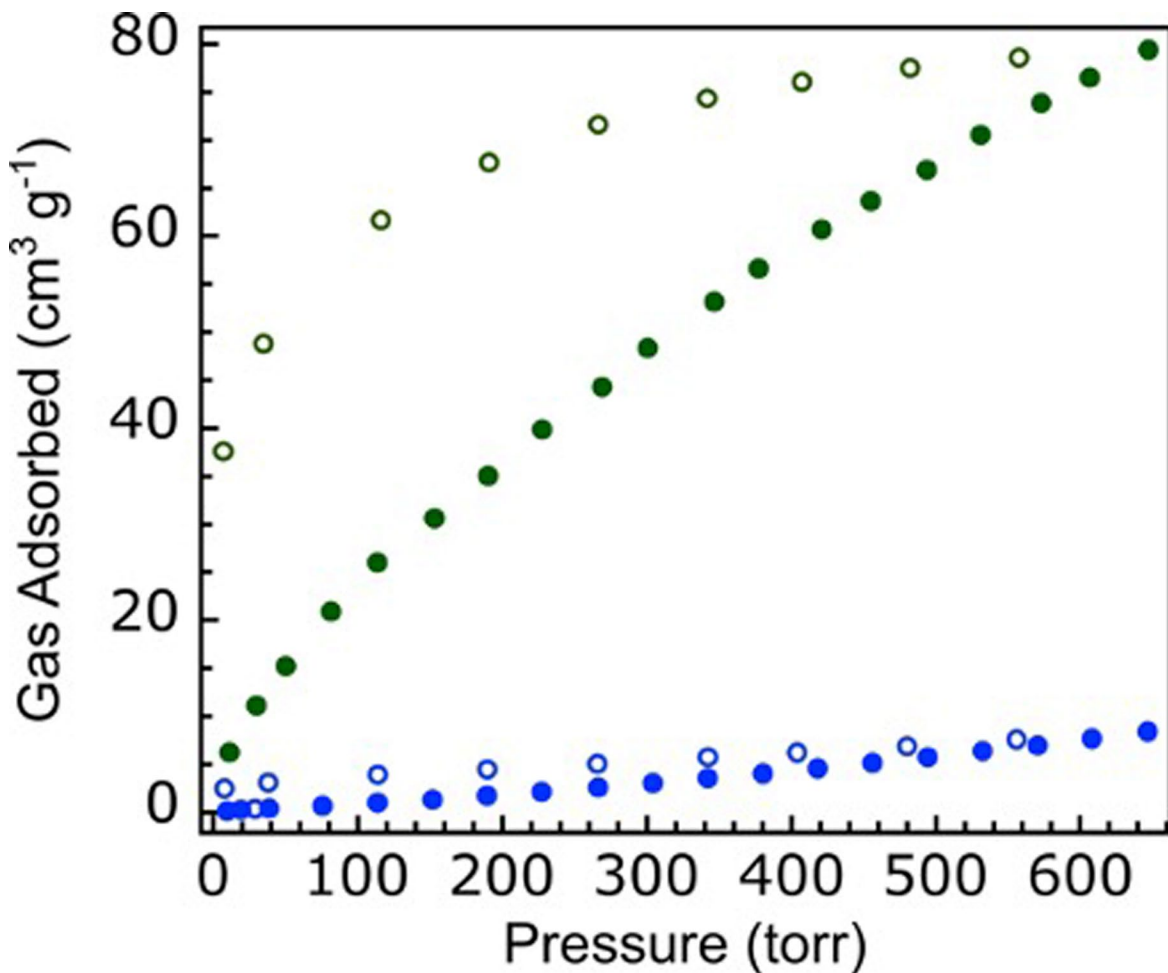
Extended Data Fig. 1 | Solid state ^{13}C NMR of PHATN. **a**, Cyclized PHATN (2) and the thermolyzed product (PHATN). Note the retention of the characteristic aromatic material peaks between δ 200-100 ppm and the disappearance of the alkyl peaks between δ 75-0 ppm, indicating the near-quantitative removal of the alkyl chains during thermolysis. **b**, Solid-state ^{13}C NMR of the PHATN material incorporated into an electrode (see Methods for details), both as-fabricated (orange trace) and soaked in electrolyte (purple trace), showing a shift assigned to ion association to a carbonyl within the material. Asterisks denote spinning sidebands at magic angle spinning frequency of 18 kHz.



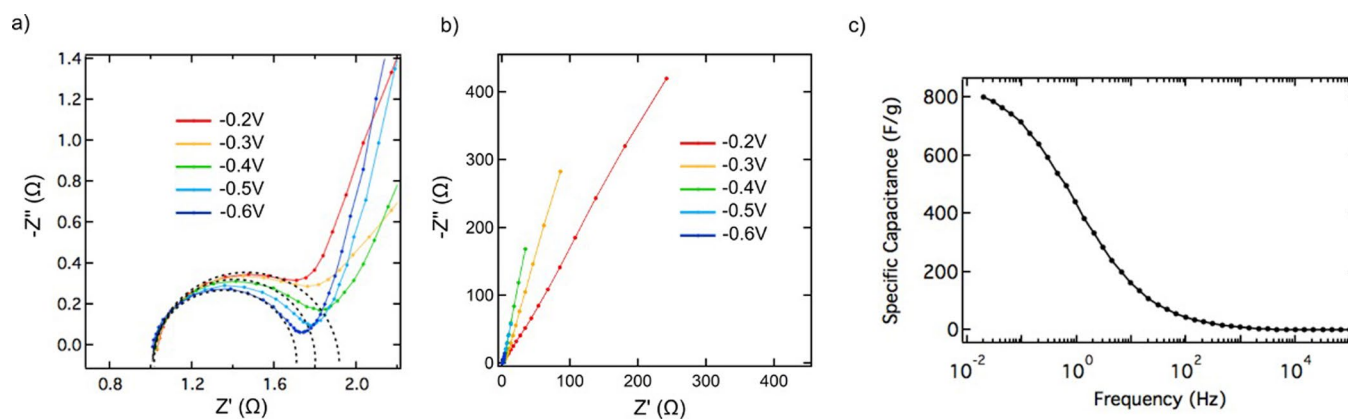
Extended Data Fig. 2 | DFT model of extended PHATN. (a) Top-view and (b) side-view of the DFT energy-minimized structure of Extended PHATN composed of multiple units of PDI and HATN. The accessible space provided by molecular contortion is clearly visible.



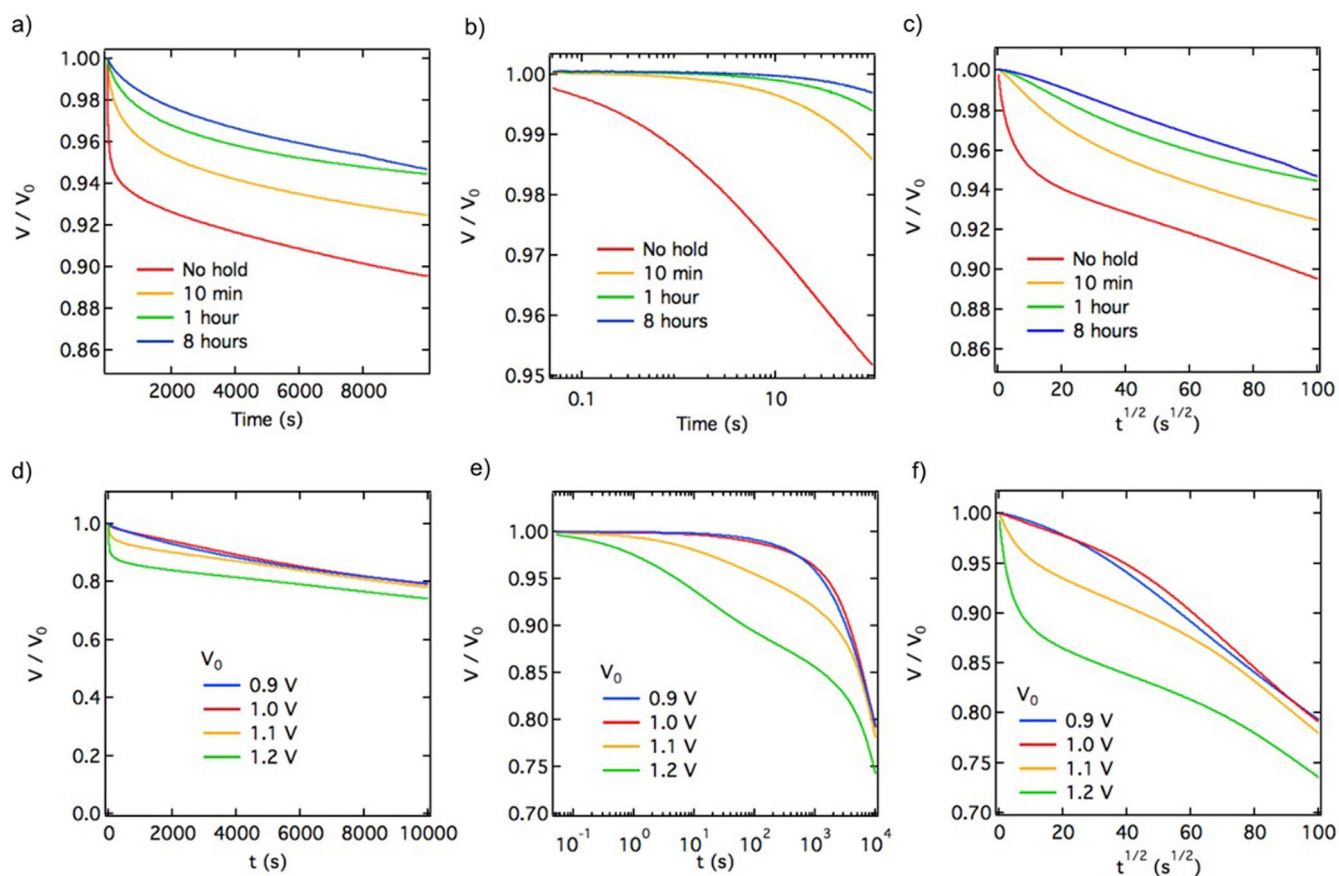
Extended Data Fig. 3 | Specific capacitance as a function of current density for PHATN and a suite of benchmark materials. Green symbols are carbon-based materials;^{35,49-51} red symbols are conducting polymer-based materials;^{5,27,31-34,52-64} purple symbols are hybrid organic/inorganic materials;⁶⁵⁻⁸² and blue symbols are inorganic materials⁸³⁻⁹². PHATN outperforms nearly all other pure organic materials at lower rates, and at higher rates achieves performance unprecedented in any material class besides inorganic compounds. PHATN values and all reference values are taken from three-electrode measurements.



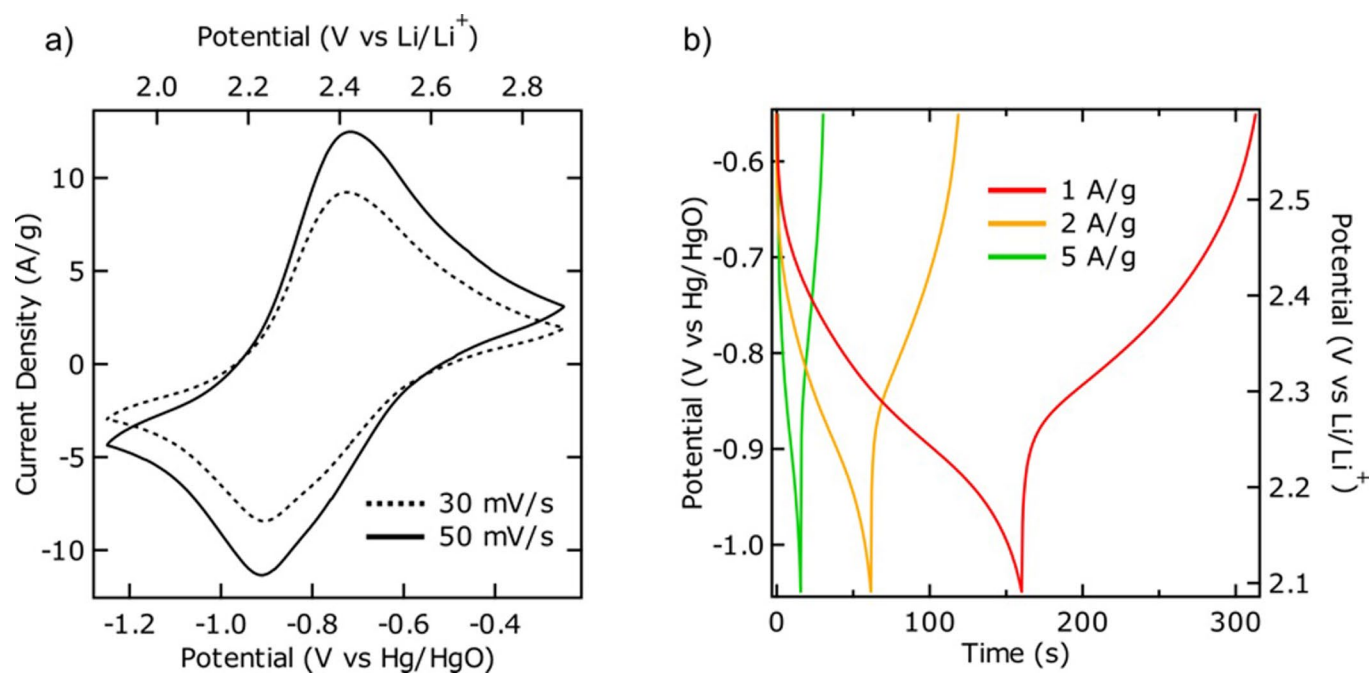
Extended Data Fig. 4 | Gas adsorption measurements of PHATN and PA-PDI. Adsorption (filled symbols) and desorption (open symbols) isotherms of CO₂ for PHATN (dark green) and PA-PDI (blue) collected at -78°C . Analysis of the PHATN isotherm (dark green) shows a Brunauer-Emmett-Teller surface area of $131\text{ m}^2/\text{g}$, calculated using the pressure range 50–227 torr, and a Langmuir surface area of $671\text{ m}^2/\text{g}$, calculated using the pressure range of 227–647 torr. However, as PHATN can likely undergo further structural distortions under operating conditions, these values are intended to be an estimate of the surface area and are included here for reporting purposes only. Analysis of the PA-PDI isotherm (blue) shows a Brunauer-Emmett-Teller surface area of $12\text{ m}^2/\text{g}$, calculated using the pressure range 50–227 torr. This is indicative of extremely low porosity, consistent with our hypothesis that contortion is crucial to the characteristic porosity shown in PHATN.



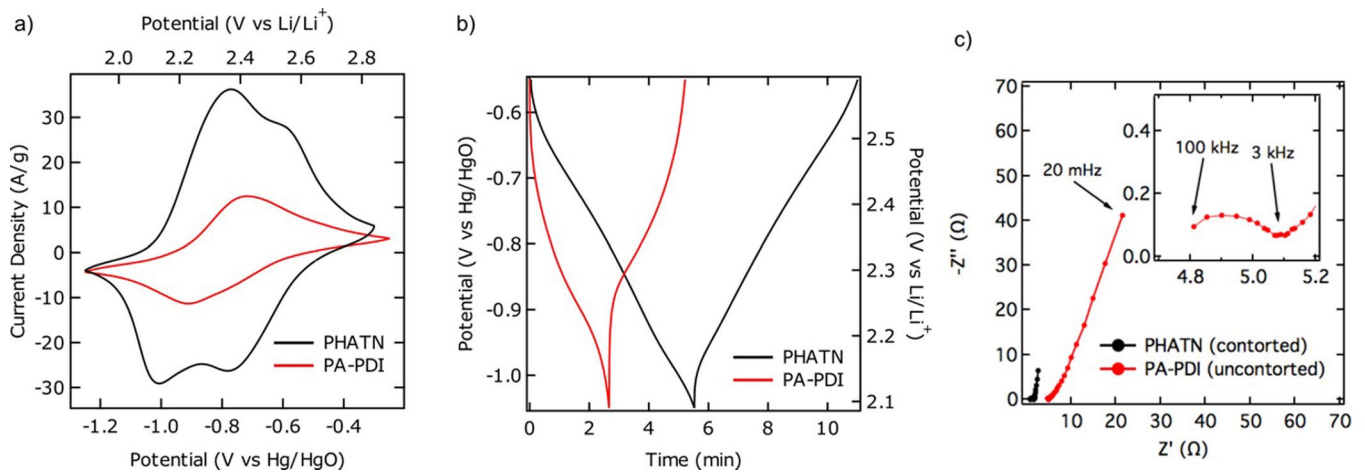
Extended Data Fig. 5 | EIS measurements of PHATN performed at a range of hold potentials. **a**, High frequency region of the Nyquist plots displaying potential dependence of the diameter of the semicircular segment. The change in diameter of the semicircle with potential is indicative of a change in charge transfer resistance, as expected from a pseudocapacitive process⁹³. The dotted lines are guides for the eye. **b**, Low frequency region of the Nyquist plots, which shows steeper Warburg regions at more negative potentials. **c**, Frequency dependence of the specific capacitance, which shows a low-frequency plateau forming near 800 F/g - near the maximum measured capacitance (689 F/g) and approaching the theoretical capacitance of the material (996 F/g). The potentials are in V vs Hg/HgO.



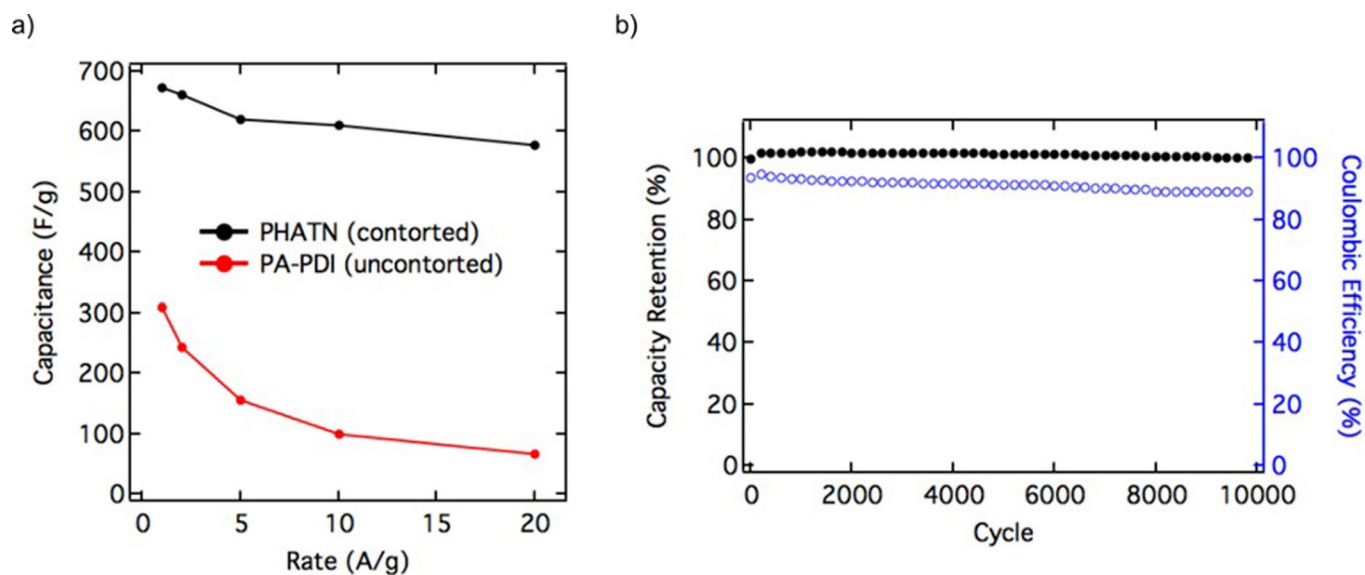
Extended Data Fig. 6 | Self-discharge of PHATN in a three-electrode configuration. (a), (b), and (c) show the effect of holding the electrode at the max charge voltage before allowing to relax, with (a) in linear time, (b) in log time, and (c) in root time. (d), (e), and (f) show the effect of the max charge voltage on the self-discharge behavior, with (d) in linear time, (e) in log time, and (f) in root time.



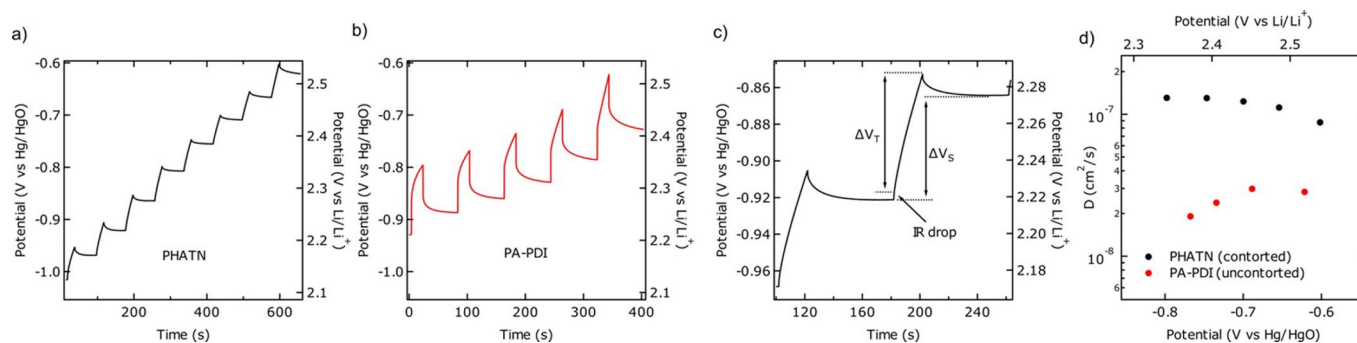
Extended Data Fig. 7 | Electrochemical characterization of PA-PDI, an uncontorted control material. **a**, CV of PA-PDI shows similar reversible redox peaks to PHATN, though sharper and less broad. **b**, GCD of PA-PDI shows relatively high IR drop and less ideal triangular capacitor shape. All measurements were performed in 6 M KOH aqueous electrolyte.



Extended Data Fig. 8 | Direct electrochemical comparison of PA-PDI with PHATN. **a**, CV at 50 mV/s and **b**, GCD at 1 A/g. **c**, Nyquist plot of PA-PDI, when compared to PHATN, displays a less steep Warburg slope in the low-frequency region, indicating less capacitive character. Both measurements are performed at -0.7 V vs Hg/HgO. Frequency range is from 100 kHz to 20 mHz.



Extended Data Fig. 9 | Rate and cycling performance of PA-PDI. **a**, Specific capacitance values vs. rate for PHATN and PA-PDI. The latter has consistently lower performance, especially at high rates, attributable to the absence of contortion and resulting internal space which enable ion movement. **b**, Capacity retention and coulombic efficiency vs. number of cycles for PA-PDI. The material maintains the same high stability over 10,000 cycles as PHATN, indicating that the polymeric material is well-formed and not affected by repeated charging and discharging.



Extended Data Fig. 10 | Galvanostatic intermittent titration technique (GITT) for PHATN and PA-PDI. GITT discharge curves as function of time for **(a)** PHATN and **(b)** PA-PDI. The measurements were performed at 2 A/g with 20 s current pulse and 1 min open circuit relaxation. **c**, Schematic interpretation of the GITT data to estimate the diffusion constant (see below equation). **d**, Diffusion coefficient (D) of the charge carrying species measured from GITT for PHATN and PA-PDI. Comparing the diffusion coefficients across the potential range, we observe that the diffusion coefficient of PHATN ($\sim 1 \times 10^{-7}$ cm²/s) is nearly one order of magnitude larger than that of PA-PDI ($\sim 3 \times 10^{-8}$ cm²/s), indicating that the charge carrying species (K^+) diffuses through the internal space created by contortion much more quickly, leading to the superior performance of PHATN. These values of ionic diffusion coefficients are comparable to reported values measured with aqueous electrolyte in porous polymeric materials^{94,95}.